RESEARCH ARTICLE | JULY 22 2025

Wave breaking characteristics around a wedge-shaped bow: High-fidelity simulation of water–air–bubble mixed flow ⊕✓

Yuming Shao (邵聿明) ; Bowei Song (宋波伟); Jianhua Wang (王建华) ✉ ; Wentao Wang (王文涛); Decheng Wan (万德成)

Check for updates

View Online   Export Citation

Articles You May Be Interested In

Global dynamics analysis of nappe oscillation

Physics of Fluids (December 2014)

Time-dependent invasion laws for a liquid–liquid displacement system

Physics of Fluids (July 2024)

Drop dynamics after impact on a solid wall: Theory and simulations

Physics of Fluids (June 2010)

AIP Publishing

Wave breaking characteristics around a wedge-shaped bow: High-fidelity simulation of water–air–bubble mixed flow Ⓕ

Yuming Shao (邵聿明),[1] ⓘD Bowei Song (宋波伟),[2] Jianhua Wang (王建华),[1,a] ⓘD Wentao Wang (王文涛),[1,3]
and Decheng Wan (万德成)[1] ⓘD

AFFILIATIONS

[1]Computational Marine Hydrodynamics Lab (CMHL), School of Ocean and Civil Engineering, Shanghai Jiao Tong University, Shanghai 200240, China
[2]Ningbo Pilot Station, Ningbo Dagang Pilotage Co., Ltd., Ningbo 315020, China
[3]China Ship Scientific Research Center, Wuxi 214082, China

[a]Author to whom correspondence should be addressed: jianhuawang@sjtu.edu.cn

ABSTRACT

Wave breaking is a complex and widely occurring phenomenon around marine structures, characterized by the coexistence of water, air, bubbles, and spray, as well as its inherently multiphase, multiscale, and multi-physics nature. This paper investigates the wave breaking of a wedge-shaped bow under various yaw angles ($\gamma = 0°$, $10°$, $15°$, $20°$, and $30°$) through high-fidelity numerical simulations. A direct forcing immersed boundary method is adopted to model the presence of the wedge-shaped bow, enabling accurate treatment of solid–fluid interaction as the structure pierces the free surface. The study employs a coupled level-set and volume-of-fluid method, along with adaptive mesh refinement techniques, to capture the severe deformation of the free surface and the characteristics of the water–air–bubble multiphase flow. The influence of yaw angle on large-scale flow structures such as wave elevation, air tube evolution, and liquid film tearing, and small-scale microstructures such as droplet splashing, air entrainment, and bubble motion is analyzed. The results show that increasing the yaw angle significantly enhances the nonlinear characteristics of bow wave breaking, leading to more intense liquid film tearing, an expanded range of air tube distribution, and the formation of secondary splashing and bubble wake mixing. The number and volume of droplets increase markedly with yaw angle, with their size distribution following a power law of -4.5. The bubble distribution is primarily influenced by vortex shear and buoyancy, with the size spectrum transitioning from $-10/3$ to -4.5 as the bubble size increases. This study reveals that yaw angle, by altering the flooding angle, impacts the bow wave-breaking mechanism, providing insights into optimizing ship hydrodynamic performance and understanding marine spray and water–air–bubble wake dynamics.

I. INTRODUCTION

In the field of marine and naval engineering, wave breaking at the bow of a ship is an inevitable occurrence during navigation, especially pronounced at high speeds. This phenomenon is caused by the obstructing effect of the ship's complex bow shape, which generates a high-pressure region at the bow, leading to the formation of a bow wave. Under the intense impact between the ship hull and the surrounding fluid, the bow wave undergoes strong nonlinear free-surface flow phenomena such as overturning, breaking, and splashing, known as bow wave breaking. This phenomenon is often accompanied by a significant amount of liquid droplet splashing and the entrainment of

large quantities of air into the water. The interaction between the bow wave and the separated flow at the stern creates a large-scale, white, water–air–bubble mixture around the structure. Additionally, the energy dissipated by the wave breaking at the bow contributes to an increase in the ship's resistance and a reduction in propulsion efficiency.[1] As a result, bow wave and breaking phenomena have attracted considerable attention from researchers in the marine field.

In the early studies of bow wave breaking, researchers typically relied on experimental observation and measurement methods to investigate and analyze the physical phenomena. Several studies[2–5] have examined the variation of bow wave characteristics at different speeds. Through techniques like high-speed photography, these studies

have recorded data on the wave-breaking patterns, revealing the distribution characteristics of bow wave breaking as a function of ship speed. Baba[6] suggested that bow wave breaking increases the total resistance of the ship, emphasizing the close relationship between wave-breaking resistance and the turbulent energy dissipation generated by the breaking of the bow wave, which is influenced by the ship's speed. Olivieri et al.[7,8] conducted towing tank experiments on the DTMB 5415 ship model at high Froude numbers, studying the impact of speed and size effects on bow wave breaking. They found that at high speeds, droplet splashing was prominent, and the overturning-type wave breaking and shoulder-breaking waves were clearly observed. Additionally, they discovered scars between overturned waves and capillary waves on the wave surface. Choi et al.[9] used high-speed cameras to study two types of ship hulls, one slender and one full-bodied, and found that bow wave breaking could be classified into plunging breaking and spilling breaking. Liu et al.[10] focused on bow wave breaking for the KCS ship model with a 1° bow trim, studying the forces on the model, the wave heights in the broken and unbroken regions, and the vorticity distribution. Their study also highlighted significant technical challenges in measuring the fluctuations of bow waves and the details of water–air mixing phenomena. Mallat et al.[11,12] used high-resolution PIV (particle image velocimetry) to study bubble sweep-down caused by bow wave breaking, providing images of the submerged portion of the breaking region, revealing the multi-scale water–air mixing phenomenon, although quantitative measurements remained challenging.

Due to the high costs of experimental equipment and the challenges of measurement techniques, combined with the advancement of computational hardware and numerical methods, many researchers have turned to numerical simulations to study bow wave breaking. At the 2025 Workshop on CFD in Ship Hydrodynamics, a dedicated session was held on the numerical simulation of KCS bow wave breaking to encourage more researchers to study this phenomenon. Bow wave breaking involves complex multi-scale, two-phase flow phenomena, such as wave breaking, droplet splashing, and bubble sweep-down, where accurate capture of the free-surface interface is crucial. Two primary methods exist for solving the two-phase fluid interface: the Lagrangian-based interface tracking method and the Eulerian-based interface capturing method. The former typically uses meshless particle methods for simulations. Landrini et al.[13] performed numerical simulations of bow wave breaking using the meshless SPH method and developed an SPH-BEM hybrid method to simulate detailed flow fields of wave breaking. Marrone et al.[14] conducted refined simulations of bow wave breaking for high-speed slender ship hulls using 3D SPH methods, modeling over 100 million particles to obtain fine details of the wave-breaking phenomenon. Chen and Bhai[15] employed the SPH method to investigate the generation and distribution characteristics of sea spray under wave action for different bow shapes. By comparing bulbous, clipper, raked, and ice resistant bows, they found that the bow geometry significantly influences the type, height, velocity, and spatial distribution of spray generated by wave breaking. However, the computational cost remained high, and meshless methods faced challenges in simulating boundary layer flows and two-phase turbulent flows.

The Eulerian-based interface-capturing method is currently the main approach for solving free-surface flow problems. There are three main methods: volume of fluid (VOF), level-set (LS), and the coupled level-set and VOF (CLSVOF) method. VOF is one of the most commonly used methods for capturing the two-phase fluid interface.[16] The key advantage of the VOF method is its ability to ensure mass conservation during the computation. Wang et al.[17,18] used the OpenFOAM platform to simulate the bow wave-breaking problem of the KCS ship at high speeds using an algebraic VOF method with artificial compression terms, achieving numerical solutions for bow wave breaking with relatively low computational costs. However, their results showed that the algebraic VOF method struggled to capture finer details, such as overturning wave breaking and air entrainment. Wu et al.[19] also used OpenFOAM and the geometric VOF method to simulate bow wave breaking for the DTMB ship model at various trim angles, confirming that trim angle significantly affects bow wave breaking. The level-set method is another common interface-capturing technique, which is better suited to calculating surface curvature compared to VOF. The free-surface position and fluid density are determined by solving the transport equation for the distance function, making it more reliable for solving surface tension in detailed micro-scale flows.[20] Wilson et al.[21] used a single-phase level-set method combined with unsteady RANS equations to simulate a high-speed transom stern ship at three different Froude numbers ($Fr = 0.25$, 0.43, and 0.62), analyzing the shape of breaking and nonbreaking waves and the vortex shedding process, achieving good resistance prediction accuracy. Carrica et al.[22] employed the single-phase level-set method with overset grids to conduct free-surface wave simulations for the DTMB 5415 ship model in different heave and trim conditions, revealing that trim angle significantly influenced the bow wave. However, their study did not capture bow wave-breaking phenomena. Mascio et al.[23] used the level-set method to simulate the free-surface flow around ships, providing a good representation of high-speed bow wave overturning but unable to capture finer details like cavities in multiple overturning waves. The CLSVOF method, which couples the level-set and VOF methods, has also been widely used for capturing violent free-surface flows.[24,25] Wang et al.[26] used the CLSVOF method to provide a high-precision solution for wave breaking, including overturning wave details, using over a billion grid points to achieve detailed free-surface flow analysis. Li et al.[27] employed the CLSVOF method to numerically simulate a surface-piercing hydrofoil, focusing on the hydraulic jump phenomena and capturing wave breaking.

The bow of a ship is a complex three-dimensional curved structure, and the factors influencing wave breaking are numerous. Therefore, simplifying the bow into simpler structures is beneficial for studying the bow wave-breaking phenomenon in greater detail. The simplest approach is to simplify the bow structure to a rectangular flat plate. Noblesse et al.,[28–31] based on dimensional analysis and towing tank experiments, proposed a linearized free-surface flow theory. This theory can determine the geometry of the bow wave under different speeds and inflow angles, but it currently only applies to conditions where the bow wave does not break. Hu et al.[32,33] performed high-fidelity numerical simulations of the flow around a flat plate under different conditions using the CSLVOF method, capturing free-surface breaking, bubble entrainment, and aerated cavity structures. Additionally, numerous researchers have studied the simplification of the bow as a thin hydrofoil structure, focusing on the formation of ventilated cavities caused by wave splashing.[34,35] Huang et al.[36] numerically studied the effect of different oblique angles on the hydrodynamic performance of surface-piercing hydrofoils. They found that at low velocity, the oblique angle has little effect on the ventilation state

but improves the lift-to-drag ratio, while at higher speeds, the oblique angle alters the ventilation state of the hydrofoil, affecting the lift and drag coefficients. Zhi et al.[37,38] investigated the formation mechanism of tip vortex-induced ventilation on surface-piercing hydrofoils, analyzing flow characteristics, hydrodynamic load changes, and the relationship between ventilation and flow structure. However, their research mainly focused on cavity formation caused by the bow wave and gave less attention to overturning wave breaking and bubble entrainment. Simplifying the ship's bow structure into a wedge-shaped body appears to be a more reasonable approach. Waniewski and co-workes[39–41] conducted experimental research on the bow wave of wedge-shaped bodies at different speeds and drafts in towing tanks. They pointed out that bow wave flow is highly nonlinear and seems to have no theoretical solution. They also attributed the jet's breakup and the bubble clouds formed to disturbances on the free surface. Karion et al.[42] performed additional experiments in a deep-water tank, discovering that wave breaking occurs when the Froude and Reynolds numbers exceed certain critical levels, with spray generation being dominated by the Weber number. Wang et al.,[43] building on Waniewski's experiments, used cartesian grids and orthogonal curvilinear grids to numerically simulate conditions with $Fr = 2.93$, studying the bow wave structure and velocity distribution at different cross sections. In our previous research,[1] we conducted a study in a circulating water tank on the factors influencing wave breaking for a wedge-shaped bow. We quantitatively summarized the effects of flow velocity, draft, flooding angle, flare angle, and yaw angle on the resistance, the broken and unbroken wave heights, and other aspects. However, due to limitations in experimental equipment, we did not study small-scale structures such as droplets and bubbles during the bow wave-breaking process.

To study small-scale structures like bubbles and droplets during wave breaking,[44,45] adaptive mesh refinement (AMR) is an effective approach for balancing computational resources and precision. Many researchers[46,47] have used AMR combined with DNS techniques to numerically simulate pure wave breaking, analyzing flow characteristics like roll waves in detail. Mostert et al.[48] studied the effects of different Reynolds and Bond numbers on the energy, bubble, and droplet statistical characteristics during wave breaking, noting that when the bubble size is smaller than the Hinze scale, the bubble size distribution follows a $-3/2$ power law, while for bubbles larger than the Hinze scale, the distribution follows a $-10/3$ power law. Wang et al.[49] used the open-source tool Gerris, employing AMR to simulate the fine-scale flow features and wave-breaking phenomena for a V-shaped ship. Yang et al.[50] used AMR in combination with the LES method for detailed simulations of wave breaking around a transom stern, applying a conservative VOF method and simulating the ship boundary with the immersed boundary method (IBM). Their study captured detailed features of wave overturning and air entrainment. These studies demonstrate that AMR can effectively capture small-scale structures within the broken waves.

In our previous research,[1] it was observed that the yaw angle and flooding angle are two prominent factors influencing bow wave breaking for a wedge-shaped bow. In addition, the influence of yaw angle can include the effect of the flooding angle. Therefore, in this study, high-fidelity numerical simulations of bow wave breaking for a wedge-shaped ship will be conducted at yaw angles of $\gamma = 0°$, $10°$, $15°$, $20°$, and $30°$. In addition to analyzing large-scale structures such as free-

surface wave height, air tube, and cavity evolution, the primary focus is to analyze the flow characteristics of small-scale microstructures such as droplet splashing, air entrainment, and bubble sweep-down. For the numerical methods, this study adopts the direct forcing immersed boundary method to model the presence of the solid structure and utilizes the CLSVOF method in conjunction with AMR technology to accurately capture the fine-scale features of the free surface. The simulation results reproduce key features of bow wave breaking for the wedge-shaped bow, including wave overturning and breaking, followed by the formation of bubbles and the rooster-tail behind the stern. Regarding the water–air–bubble mixture flow resulting from wave breaking, this study presents a detailed analysis based on the statistical characteristics and spatiotemporal distribution of bubbles and droplets.

The structure of this study is outlined as follows: In Sec. II, the numerical methods employed will be introduced, including the governing equations, free-surface capture method, and immersed boundary method. The numerical model for the physical problem under investigation will then be established, and the computational grid will be verified in Sec. III. Based on this, detailed analysis of the flow field results will be conducted, including the main flow structures, droplets, entrained air, entrained bubbles, and turbulent vortex structures in Sec. IV. Finally, the results of this study will be summarized in Sec. V.

II. NUMERICAL METHOD

A. Governing equations

This study is based on the open-source two-phase flow solver Basilisk,[51] which is a development of Gerris.[52] The solver has been widely applied to various multiphase flow problems, including pure wave breaking,[46,48] jet dynamics,[53] droplet dynamics,[54] shallowly submerged hydrofoils,[55,56] shallowly submerged cylinders,[57] cylinder wake flow,[58] and ship bow wave breaking.[59]

For incompressible fluids, the governing equations are

$$\rho(\partial_t \mathbf{u} + (\mathbf{u} \cdot \nabla)\mathbf{u}) = -\nabla p + \nabla \cdot (2\mu \mathbf{D}) + \rho \mathbf{g} + \mathbf{f}_\sigma + \mathbf{f}_{\mathrm{IB}}, \quad (1)$$

$$\nabla \cdot \mathbf{u} = 0, \quad (2)$$

where $\mathbf{u}$ represents the fluid velocity, ρ is the density, p is the pressure, μ is the dynamic viscosity, $\mathbf{g}$ is the gravitational acceleration, and $\mathbf{D} = (\nabla \mathbf{u} + \nabla \mathbf{u}^T)/2$ is the deformation tensor. $\mathbf{f}_\sigma$ accounts for surface tension effects, while $\mathbf{f}_{\mathrm{IB}}$ represents the solid effects in the immersed boundary method. A large eddy simulation (LES) turbulence model is employed, where only the large energy-carrying eddies are fully resolved, while small-scale dissipative eddies are modeled using a subgrid-scale model. The Vreman eddy-viscosity model[59,60] is selected for use in this study.

B. Interface modeling

In this study, the coupled level-set and volume-of-fluid (CLSVOF) method is employed to capture the free surface, which has been previously applied to hydrofoil wave-breaking simulations.[55,56] This method provides both good mass conservation and accurate interface geometry. The convective equation is given by

$$\partial_t f + \nabla \cdot (f \mathbf{u}) = 0, \quad (3)$$

$$\partial_t \phi + \nabla \cdot (\phi \mathbf{u}) = 0, \quad (4)$$

where f represents the volume fraction in the VOF-PLIC method and ϕ is the distance function used in the level-set method.

For small-scale structures, such as bubbles and droplets, surface tension plays a crucial role in their formation and evolution and thus needs to be carefully considered.[61] To further demonstrate this point, a three-dimensional Stokes wave breaking case is provided in the Appendix. In this study, the continuous surface force (CSF) model is employed, and the surface tension term can be expressed as

$$\mathbf{f}_\sigma = \sigma\kappa(\phi)\delta_s\mathbf{n}, \tag{5}$$

where σ is the surface tension coefficient and δ_s is the Dirac delta function of the interface, indicating that the surface tension term acts on the interface. $\mathbf{n}$ is the normal vector to the interface, and $\kappa(\phi)$ is the interface curvature, defined as

$$\mathbf{n} = \frac{\nabla\phi}{|\nabla\phi|}, \tag{6}$$

$$\kappa(\phi) = \nabla\cdot\left(\frac{\nabla\phi}{|\nabla\phi|}\right). \tag{7}$$

C. Immersed boundary method

The direct forcing immersed boundary method[62,63] is implemented to account for the presence of the wedge-shaped structure, thereby extending the applicability of the multiphase Basilisk flow solver to problems involving solid structures. Without considering contact angle models, the direct forcing method has been successfully applied in studies of wave breaking induced by various structures.[27,32,33,50] Compared to the embedded boundary method already integrated into Basilisk[64] and the simple splitting method,[59,65] the direct forcing approach enhances fluid–structure interaction modeling while remaining compatible with OpenMPI-based parallelization. It is particularly suitable for scenarios involving structure piercing through the free surface in two-phase flows.[66] The method simulates the effect of the wedge on the flow field by introducing the artificial forcing term $\mathbf{f}_{IB}$ into the momentum equation on the right-hand side. As shown in Fig. 1(a), the grid points are classified into three types: (1) Solid points: grid points located inside the solid structure or on its surface; (2) Forcing points: grid points within the fluid domain that have at least

FIG. 1. Schematic diagram of the immersion boundary method about (a) division of grid points and (b) forcing point interpolation strategy.

one neighboring grid point inside the solid structure; and (3) Fluid points: grid points located within the fluid domain but not classified as forcing points. At each time step, the forcing term is used to reconstruct the velocity field at the forcing points, based on the boundary conditions of the solid. A simple and efficient interpolation method is used, as illustrated in Fig. 1(b).

For this case, for forcing point P_{IB}, P_S represents the nearest point on the solid surface, while P_{ext} is the intersection point where the line extending from P_S to P_{IB} intersects the centerline of the adjacent grid cell on the right. The velocity at the forcing point P_{IB} is given by

$$\mathbf{u}_{IB} = \frac{h_2 - h_1}{h_2}\mathbf{u}_S + \frac{h_1}{h_2}\mathbf{u}_{ext}, \tag{8}$$

where h_1 represents the distance from P_S to P_{IB}, and h_2 represents the distance from P_S to P_{ext}. These distances can be calculated based on the geometric coordinates of the points.[64,67,68]

III. COMPUTATIONAL SETUP

A. Physical model

The geometry of the wedge-shaped bow and the computational domain is shown in Fig. 2. The side length of the wedge is $L = 0.75\,\text{m}$, the total height is $H = 0.5\,\text{m}$, and the draught is $d = 0.075\,\text{m}$. The flooding angle θ refers to half the angle at the leading edge of the wedge, which is set to $15°$. The yaw angle γ refers to the angle between the longitudinal profile of the wedge and the incoming flow direction. In this study, we investigate the conditions for yaw angles $\gamma = 0°$, $10°$, $15°$, $20°$, and $30°$. The incoming flow velocity u_0 is set to 2.5 m/s, consistent with the experimental setup.[1]

The entire computational domain is composed of a cube with side lengths $L_x = L_y = L_z = 2.5\,\text{m}$, where X axis ranges from -0.3 to 2.2 m, Y axis ranges from -0.5 to 2.0 m, and Z axis ranges from -1.25 to 1.25 m. The wedge is rotated counterclockwise about the coordinate origin in the XOY plane to achieve different yaw angles. The upstream-facing side is shown in the right view of the wedge, whereas the downstream-facing side is presented in the left view. The plane at $x = -0.3\,\text{m}$ is defined as the inlet boundary, where the incoming flow velocity u_0 is imposed using a Dirichlet boundary condition. The plane at $x = 2.2\,\text{m}$ is defined as the outlet boundary, where a Neumann boundary condition is applied to the velocity. The remaining boundary conditions are set as slip wall conditions. The initial water distribution is in the region $z \leq 0$, with an initial velocity of u_0.

B. Physical parameter

The physical properties are set to match the experimental conditions: the density ratio of air to water is $\rho_a/\rho_w = 1/998$, and the dynamic viscosity ratio is $\mu_a/\mu_w = 1.784\times10^{-5}/1.138\times10^{-3}$. The gravitational acceleration is $g = 9.8\,\text{m/s}^2$, directed in the negative Z direction. The surface tension coefficient is 0.0734 N/m. The Reynolds number is $Re = \rho_w u_0 L/\mu_w = 1.64\times10^6$, and the Froude number is $Fr = u_0/\sqrt{gL} = 0.92$. The time is nondimensionalized using $t^* = tu_0/L$, where t is the computational time. Details of the bubble–droplet identification algorithm are provided in the Appendix. To facilitate analysis, several statistical formulas for the characteristics of bubbles (or droplets) are defined[27,50,56]
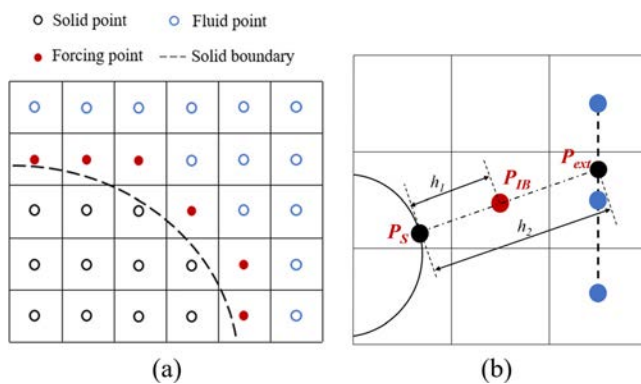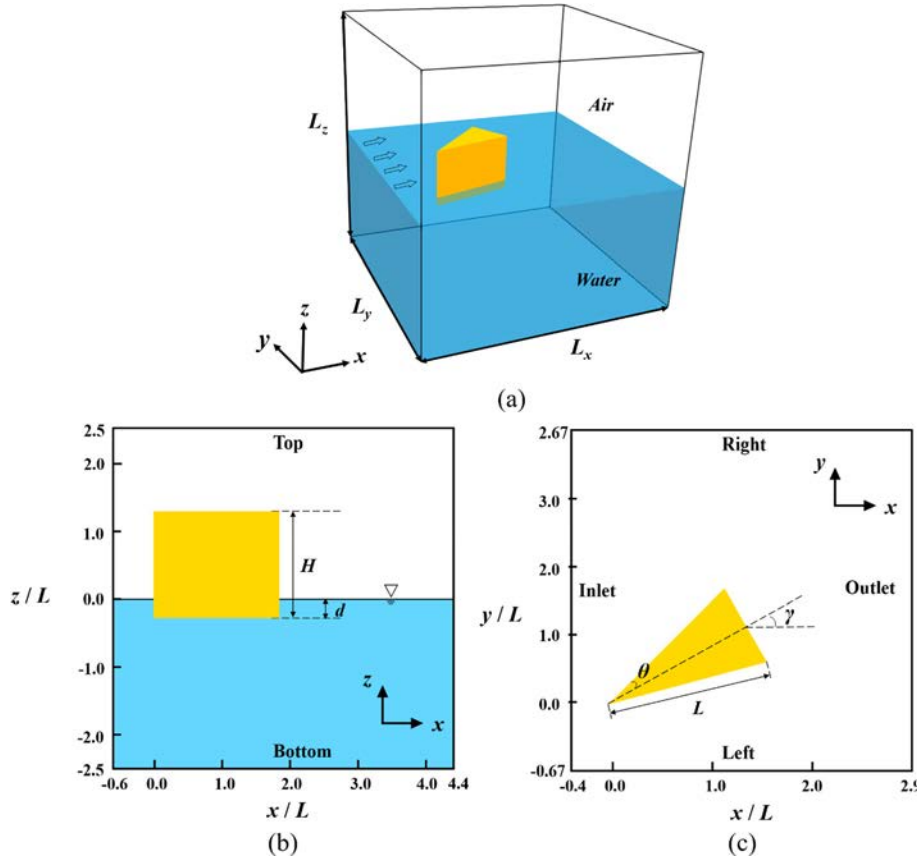
FIG. 2. Schematic diagram of physical model setup about (a) overall view, (b) side view, and (c) top view.

$$r_{eff} = \left(\frac{3v}{4\pi}\right)^{\frac{1}{3}}, \tag{9}$$

$$\overline{N}(r_{eff}) = \frac{1}{\Delta t}\int_{t}^{t+\Delta t}\frac{n(r_{eff},b)}{b}dt, \tag{10}$$

$$\overline{N}_0 = \int_{0}^{r_{max}}\overline{N}(r;b)\frac{4}{3}\pi r^3 dr, \tag{11}$$

$$\lambda_n(x,y) = \frac{1}{\Delta t}\int_{t}^{t+\Delta t}\frac{n(x,y)}{N}dt, \tag{12}$$

where the equivalent radius r_{eff} of a bubble is calculated using the volume v of the single bubble. $\overline{N}(r_{eff})$ is the change in the number of bubbles per unit volume for each millimeter of equivalent radius. This is also referred to as the time-averaged bubble size spectrum and is defined as the number of bubbles $n(r_{eff},b)$ within a bin size b, averaged over the sampling time Δt, and normalized by the total volume of entrained bubbles $\overline{N}_0$. The bin size b is chosen to be 0.1 mm. $\lambda_n(x,y)$ represents the spatial distribution density of bubbles, where $n(x,y)$ is the number of instantaneous bubbles detected within the sampling interval $x \leq x \leq x + \Delta x, y \leq y \leq y+$, $\Delta x = \Delta y = 0.01$ m. The sampling time for this study is between $t^* = 10$ and $t^* = 16$.

C. Mesh details and verification

For turbulent flows involving intense gas–liquid interactions, the importance of grid resolution is further demonstrated by an additional rising bubble case study included in the Appendix. In this study, the Basilisk flow solver's built-in octree mesh adaptivity technique is employed.[52] This method uses a wavelet algorithm to compute the estimation of numerical errors in the spatial discretization, allowing for the refinement or coarsening of grids in specific regions. Different criteria are set based on the physical phenomena of interest. Following previous studies on wave breaking,[46,48,55,56] this research sets the maximum tolerated estimated error for the volume fraction field and the velocity field of water, specifically $f = 1 \times 10^{-18}$ and $u_w = 0.4\,u_0$. These criteria are designed to refine the grid in regions with significant free-surface motion and large turbulence fluctuations beneath the water surface. As shown in Figs. 3(a) and 3(c), the regions with free-surface splashing and bubble distribution are well-resolved with finer grids. To avoid the backflow phenomenon at the outlet boundary, the mesh is coarsened in the 0.1 m range near the outlet. Additionally, to ensure the smoothness of the object surface, the same grid refinement level is applied to the surface of the wedge-shaped bow.

Using AMR technology, the grid resolution is defined as $\Delta = L_x/2^l$, where l represents the mesh refinement level. Based on previous studies of wave breaking caused by surface-piercing structures,[27,32,33,50] and considering the characteristic length of the current wedge shape, a grid resolution of around 4–8 mm is sufficient to capture the evolution of the free surface. Thus, we initially choose $l_{min} = 6$ and simulate three different mesh resolutions with $l_{max} = 8$, 9, 10, corresponding to maximum grid resolutions of 9.76, 4.88, and 2.44 mm, respectively, for the most intense wave-breaking condition $\gamma = 30°$. The
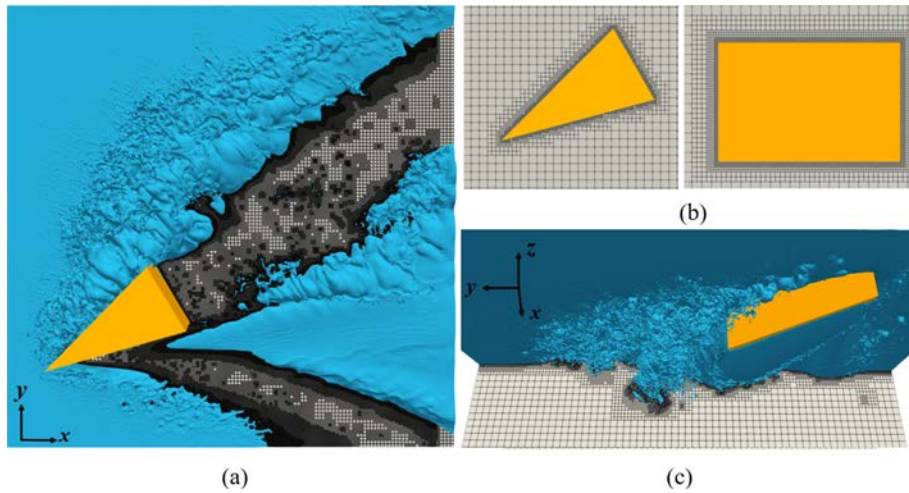
FIG. 3. The diagram of mesh adaptive refinement. Mesh refinement near (a) the free surface, (b) the surface of the wedge, and (c) underwater bubbles.

result of wave profiles on the surface of the wedge-shaped bow is shown in Fig. 4. From the figure, it can be observed that the wave profiles at the three refinement levels show consistent trends, with the curves for $l_{max} = 10$ and $l_{max} = 9$ being closer to each other, while the $l_{max} = 8$ curve is slightly lower. This discrepancy is likely because the $l_{max} = 8$ captures most of the wave features, but fails to resolve finer disturbances on the wave surface. Therefore, $l_{max} = 9$ is considered the optimal balance between computational accuracy and resource efficiency, as it results in 512 grid points per unit length, which is also sufficient for studies on wave breaking of stern[69] and scientific research ship.[59]

Numerical results for the wave profile along the wedge surface are compared with experimental data in Fig. 5. For yaw angles $\gamma = 0°$, 10°, 15°, and 20°, the wave height along the wedge side remains nearly steady. The root mean square errors of the corresponding wave heights in the experiment are 1.732, 1.742, 2.249, and 2.744 mm, respectively.[1] The simulation results show good overall agreement with the experiments, further confirming the applicability of $l_{max} = 9$. The grid

configurations for all computed conditions are listed in Table I. For the $l_{max} = 9$, the corresponding uniform grid requires $512 \times 512 \times 512$ grid number. However, with AMR, even for the most intense $\gamma = 30°$ condition, about 5×10^6 grid number are needed, greatly saving computational resources. For the $l_{max} = 10$, only the $\gamma = 30°$ condition is simulated, with the grid number reaching up to approximately 26×10^6. For subsequent analysis, all comparisons of different yaw conditions use the $l_{max} = 9$ results, while for detailed analysis of small-scale structures such as bubbles and droplets for $\gamma = 30°$ condition, the higher resolution with $l_{max} = 10$ is employed.

IV. RESULTS AND DISCUSSION
A. Free-surface flows

Figure 6 illustrates the primary free-surface evolution during bow wave breaking at a yaw angle of $\gamma = 30°$. Initially, the flow climbs along the surface of the wedge and spreads rearward along its
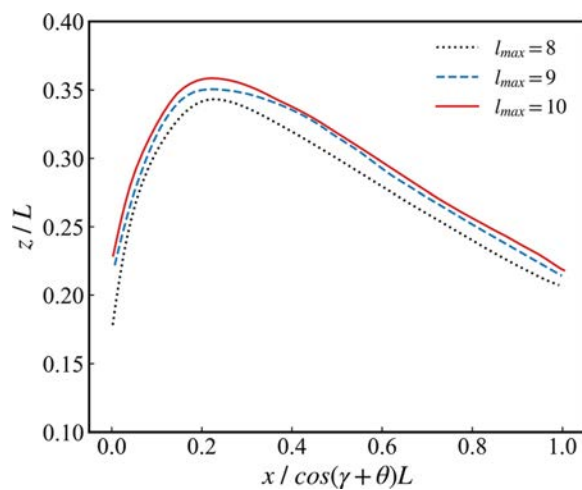

FIG. 4. The result of wave profile under different maximum refinement levels for $\gamma = 30°$.
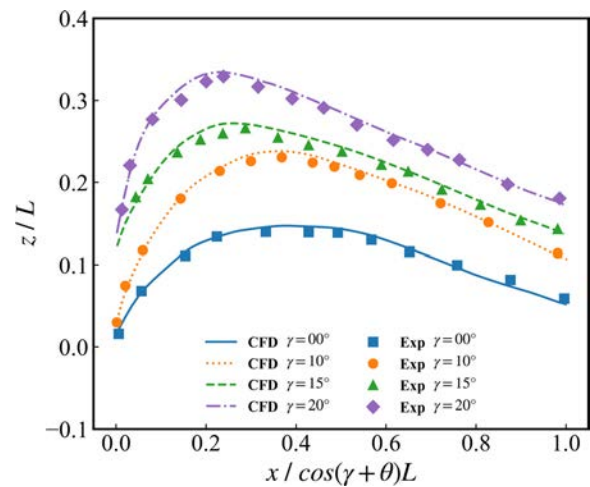

FIG. 5. Comparison of the wave profile with the experimental results under $l_{max} = 9$.

TABLE I. Grid configuration for simulation conditions.

Yaw angle (°)	l_{max}	Minimum grid size (mm)	Total grid number ($\times 10^6$)
0	9	4.88	3.41–3.44
10	9	4.88	3.60–3.67
15	9	4.88	3.82–3.88
20	9	4.88	4.23–4.32
30	8	9.76	1.21–1.24
30	9	4.88	5.18–5.35
30	10	2.44	25.74–26.07

sidewalls, as shown in Fig. 6(a). At $t^* = 1.6$, wave accumulation on the wedge surface intensifies. Under the influence of gravity, the flow rolls over away from the wedge, resulting in plunging impacts on the free surface. The jets are observed to splash into the air behind the wedge, while an air cavity forms beneath the wedge structure. As shown in Fig. 6(c), the large incoming angle causes the front wave crest to tear into thin liquid sheets. Wave overturning and breaking further induce secondary splashing into the air and the formation of longer air tubes beneath the surface. As the wave continues to accumulate energy, the flow accelerates, and the height of secondary splashing increases, as illustrated in Fig. 6(d). Eventually, the pronounced secondary plunging fades, replaced by repeated low-height overturning and breaking, which generates abundant white water, as seen in Fig. 6(e). Subsurface air tubes break into a fragmented bubbly mixture, forming three distinct bubble wakes observable in the downstream region.

Time-averaged wave elevations for five different yaw angles are extracted and presented in Fig. 7. On the upstream-facing side of the wedge, the wave-breaking region expands with increasing yaw angle due to the enhanced flooding angle. In all five cases, two prominent scars formed by plunging wave crests are observed. As the yaw angle increases, the wave amplitude becomes larger, particularly in the first plunging region. On the downstream-facing side of the wedge, the regular wave pattern gradually diminishes with increasing yaw angle. Instead, two spray waves emerge, with a noticeable surface depression forming between them. In the region behind the wedge, the transom stern induces a characteristic wave pattern in which the wave elevation first increases and then decreases downstream, forming what is commonly referred to as a rooster tail.[50,69] At lower yaw angles, wave troughs appear on both sides of the rooster tail. As the yaw angle increases, the trough on the downstream-facing side vanishes, while a deeper trough forms directly behind the stern. Although the position of the rooster tail remains relatively unchanged, its structure becomes increasingly asymmetrical. Overall, larger yaw angles result in more extensive and intense wave breaking. Nonlinear phenomena become more pronounced, accompanied by significant fluctuations in free surface elevation, as reflected by the unsmooth wave shape in the upstream-facing plunging region shown in Fig. 7(e).

Wave breaking on the upstream-facing side of the wedge is highly complex. Based on both experimental observations[1,9] and numerical results,[17,19] a schematic diagram has been constructed to illustrate the dominant flow structures associated with bow wave breaking at high Froude numbers, as shown in Fig. 8. As the incoming flow interacts with the wedge surface, a liquid sheet forms and subsequently rolls up

under the influence of gravity, generating a plunging wave jet. This wave jet also is prone to fragmentation, leading to the generation of droplets. Upon impacting the free surface, the plunging jet produces splashing droplets, and the impact region is characterized by the formation of a scar. During the plunging process, a substantial amount of air becomes entrained, resulting in the formation of air cavities or tubular structures beneath the surface. Both the edge and surface of the wave exhibit highly unsteady and turbulent motions. From a frontal perspective, this manifests as widespread white water on the right and rear sides, away from the wedge.

The surface wave profiles on the upstream-facing side of the wedge obtained from both experiments and simulations are shown in Fig. 9. Overall, the simulated results are in good agreement with the experimental measurements in terms of waveform. It is evident that larger yaw angles result in higher wave crests, which also corresponds to the intensity of wave breaking. In combination with Fig. 5, it can be further observed that increasing the yaw angle causes the wave peaks to appear higher and further upstream. Additionally, stronger instability is present at the wave edges. As shown in Figs. 9(c) and 9(d), liquid sheet tearing occurs before the wave crest, producing droplets. This behavior is consistent with the wave generation patterns observed on rectangular plates[30,32] and plate hydrofoils[34,36] under varying yaw angles.

Figure 10(a) presents the wave profile evolution at $x/L = 0.35$ cross section for the high-resolution case with $\gamma = 30°$, providing a clearer understanding of the plunging wave dynamics. At $t^* = 1.3$, the transverse wave profile begins to roll up. At $t^* = 2.3$, the plunging wave impacts the free surface, leading to a distinct entrainment of air, which appears as a regular, near-circular cavity. Also, secondary splashing is also observed. At $t^* = 16$, the splashing becomes chaotic and irregular, with multiple jets forming. The air cavity becomes smaller and loses its symmetry. Furthermore, bubbles are observed near the contact region between the wave and the wedge,[70] attributed to disturbances caused by the tearing of the leading liquid sheet. These disturbances generate pronounced undulations along the wave surface in the streamwise direction, producing numerous surface wrinkles rather than the smoothed profiles often obtained using Reynolds-averaged methods in previous bow wave studies.[10,17–19]

On the upstream-facing side, the air tube is identified as the primary flow structure responsible for air entrainment during wave breaking. The time-averaged spatial distribution of air cavities under different yaw conditions is shown in Fig. 11. The wave jet, driven by gravity, overturns toward the rear of the wedge and impacts the free surface. During this overturning process, a scar forms on the free surface, and a large amount of air is entrained beneath the surface and transported downstream, forming the air tube. As illustrated in Fig. 11(b), the top view reveals that the air tube initially spreads obliquely rearward at a relatively large angle. This region is composed of the leading edge of the wave jet and the liquid sheet attached to the wedge surface. Since it remains connected to the atmosphere, this portion is strongly influenced by the yaw angle of the wedge, which essentially alters the flooding angle. The turning point in the spatial pattern of the air tube occurs at the location where the wave jet initially plunges into the free surface. Downstream of this point, a semi-closed cavity structure forms beneath the surface, resembling a tube with a narrowing followed by widening radius when viewed from top. A comparison across the five yaw conditions indicates that with increasing
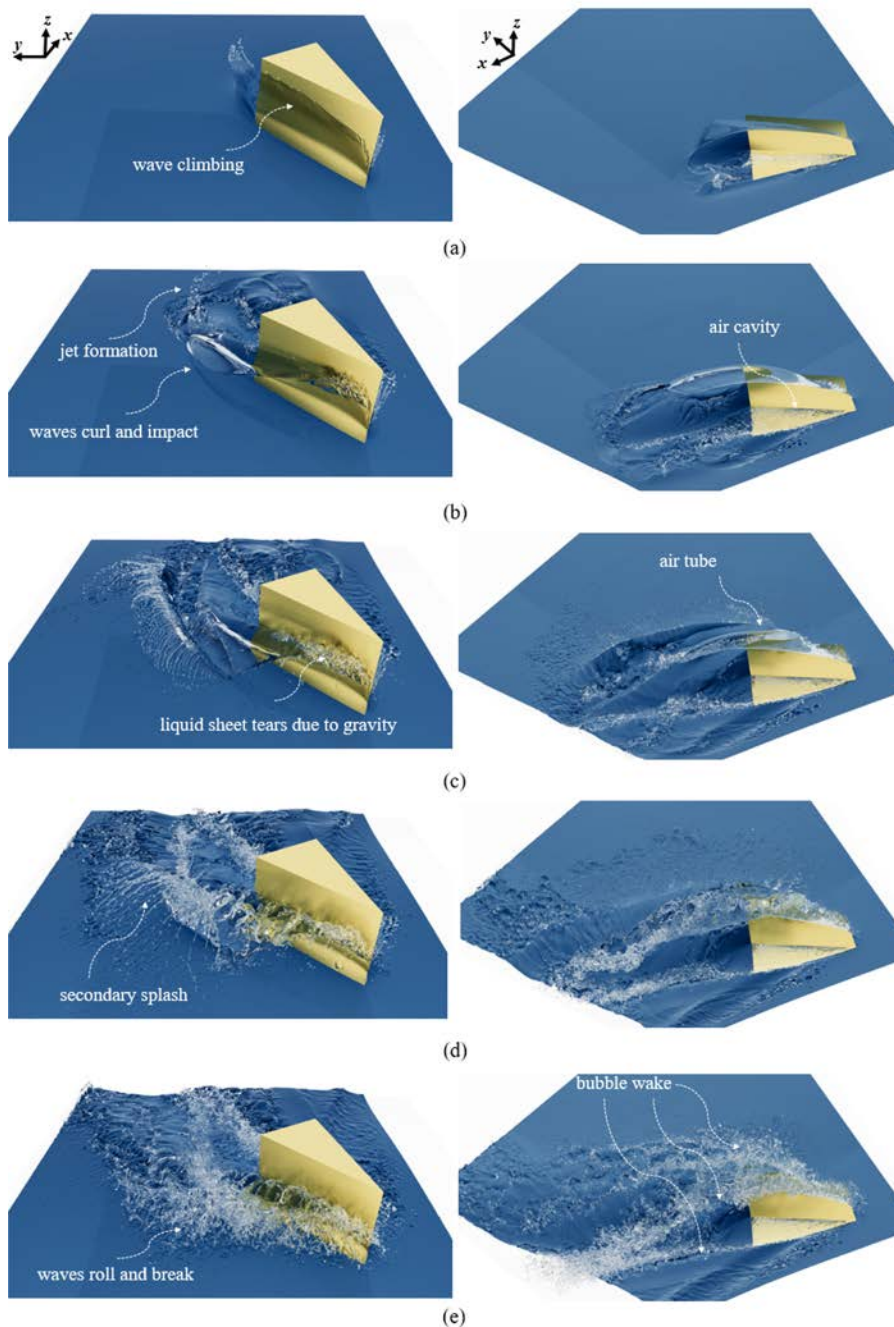
FIG. 6. Evolution of free-surface breaking for case $\gamma = 30°$ at (a) $t^* = 0.6$, (b) $t^* = 1.6$, (c) $t^* = 2.3$, (d) $t^* = 3.2$, and (e) $t^* = 6.2$.

yaw angle, the initial section of the air tube becomes larger and is distributed at a wider angle. Additionally, the initial jet impact point shifts to smaller x and larger y coordinates. For the second part of the air tube analysis, the streamwise orientation of the air tube in the X-Y plane is quantified. The streamwise angle is measured between the X-axis and the line connecting the midpoint between the jet impact initiation point and the nearest point of the opposite-side air tube, and the distal tip of the air tube. The measurements indicate that the

streamwise angles corresponding to yaw angles $\gamma = 0°$, $10°$, $15°$, $20°$, and $30°$ are $19.7°$, $21.3°$, $23.5°$, $26.3°$, and $28.1°$, respectively. These results demonstrate an increase in the streamwise orientation angle with increasing yaw angle. As shown in Fig. 11(c), the side view in the X–Z plane clearly displays the underwater structure of the air tube. A larger yaw angle results in deeper penetration and a wider vertical distribution. The free surface exhibits a downward and oblique concave profile, similar to the behavior observed when a liquid jet enters a
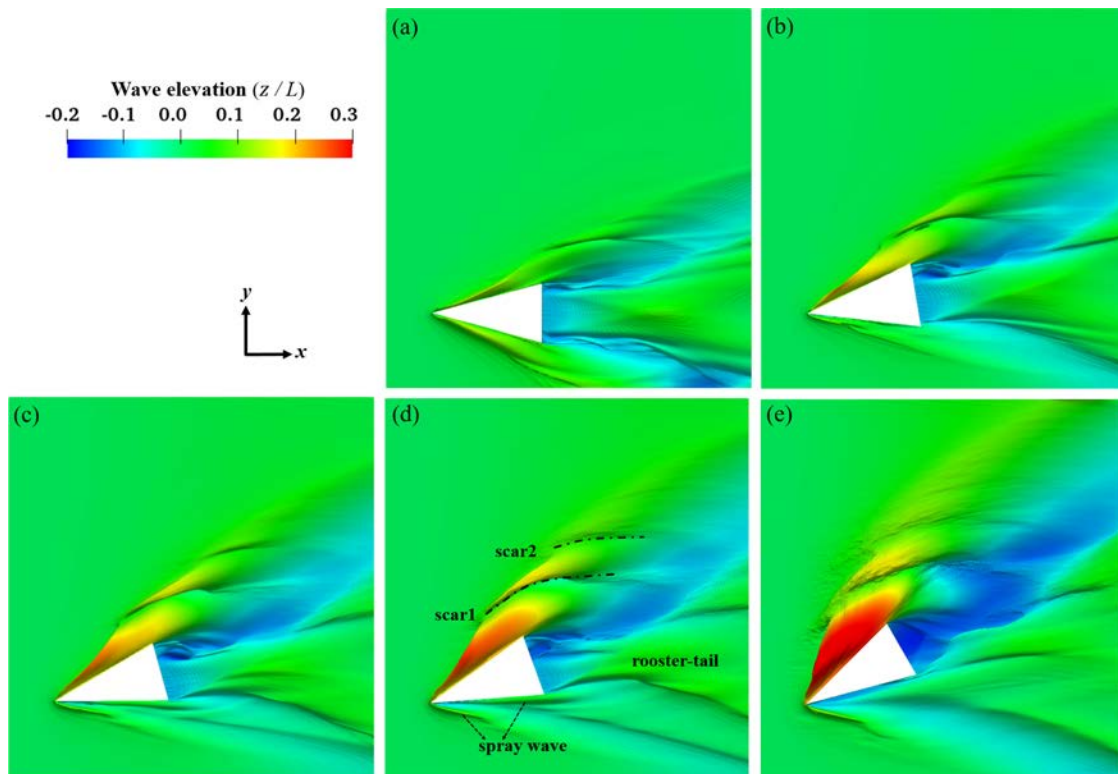
FIG. 7. Time-averaged contours of the wave elevation for yaw angles (a) $\gamma = 0°$, (b) $\gamma = 10°$, (c) $\gamma = 15°$, (d) $\gamma = 20°$, and (e) $\gamma = 30°$.
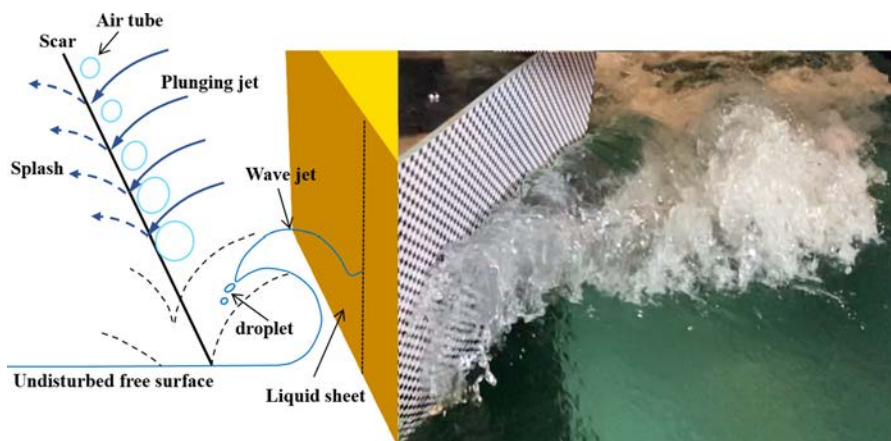

FIG. 8. Diagram of the plunging wave breaking on the upstream-facing side of a wedge.

water body at an angle,[71] driven by the initial jet velocity and gravity. The sweep-down angle of the air tube in the X–Z plane is evaluated as the angle between the X axis and the line connecting the jet impact initiation point to the distal end of the air tube. Measurements show that for yaw angles $\gamma = 0°$, $10°$, $15°$, $20°$, and $30°$, the corresponding sweep-down angles are $9.6°$, $14.6°$, $19.60°$, $24.7°$, and $27.3°$, respectively. As the yaw angle increases, the air tube exhibits a more pronounced downward sweep.

Figure 12 presents the flow features observed on the downstream-facing side. As seen in Fig. 7, two distinct spray waves are generated on the left side of the wedge. Spray wave 1 primarily originates from the interaction between the leading edge of the wedge and the incident free-surface flow. Spray wave 2 is mainly formed by the interaction between the lower leading edge and the incoming flow.[1] At the junction of these two spray waves near the wedge's leading edge, an air-ventilated cavity emerges, referred to as air-ventilated cavity 1.
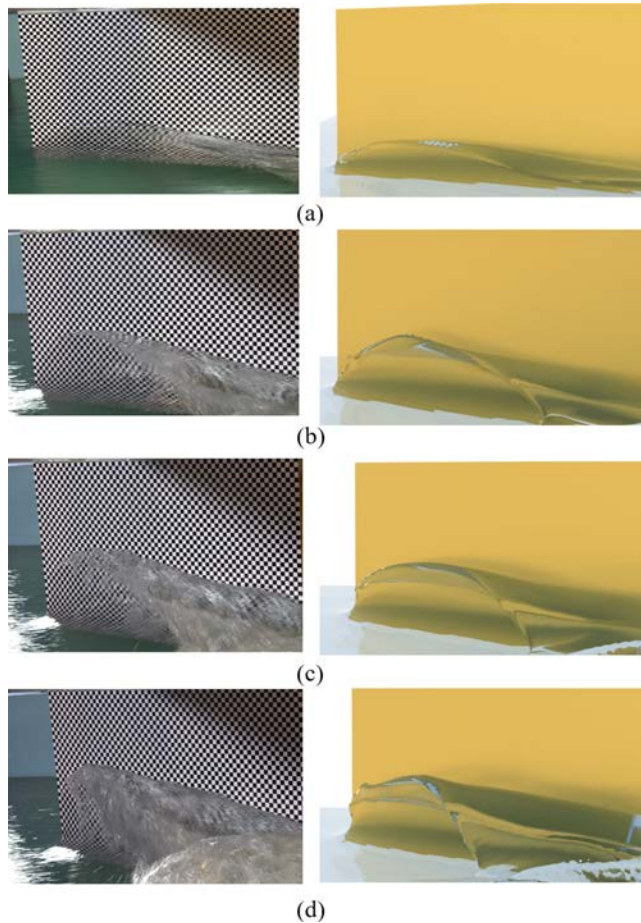
FIG. 9. Comparison of the experimental results (left) and numerical results (right) of the wave profile on the upstream-facing side for yaw angles (a) $\gamma = 0°$, (b) $\gamma = 10°$, (c) $\gamma = 15°$, and (d) $\gamma = 20°$.

As depicted in Fig. 12(b), the spatial extent of air-ventilated cavity 1 along the wedge surface increases with the yaw angle and gradually spreads toward the lower surface of the wedge. For the case of $\gamma = 20°$, the cavity nearly reaches the bottom edge of the wedge. Additionally, another air-ventilated cavity is observed near the lower rear region of the wedge, denoted as air-ventilated cavity 2. With increasing yaw angle, air-ventilated cavity 2 advances forward along the bottom surface. As shown in Fig. 12(c), for the $\gamma = 30°$ case, where wave breaking is most intense, air-ventilated cavity 2 evolution is illustrated at various time instances. At $t^* = 0.2$, air-ventilated cavity 1 has already extended significantly toward the bottom of the wedge. At $t^* = 0.63$, air-ventilated cavity 1 and 2 merge beneath the wedge. At $t^* = 3$, a fully ventilated cavity is formed along the entire bottom surface, with air openings at both the front and rear ends. This phenomenon is analogous to the ventilation mechanism induced by leading-edge and trailing-edge separation on high-speed hydrofoils[34–38] and is influenced by factors such as draft, oblique angle, and flow velocity.

To facilitate the analysis of energy variation during the wave-breaking process, the energy of the water body within the computational domain is extracted

$$E_k = \frac{1}{2} \int \rho \mathbf{u}^2 \, dx\, dy\, dz, \quad (13)$$

$$E_p = \int \rho \mathbf{g} z \, dx\, dy\, dz, \quad (14)$$

$$E_t = E_k + E_p, \quad (15)$$

where E_k is kinetic energy, E_p is potential energy, and E_t is the total energy.

Figure 13(b) presents the evolution of kinetic energy, where all cases exhibit a similar trend. As the initial velocity of the water body is assigned as the inflow velocity, a decrease in total velocity is observed at the early stage $t^* \leq 1$ due to obstruction by the wedge-shaped body. During the subsequent wave-breaking stage, the kinetic energy rises sharply. Except for the case with $\gamma = 30°$, all other conditions reach a steady state by $t^* = 6$, while the $\gamma = 30°$ case stabilizes at $t^* = 10$, with its kinetic energy approximately 2.6–3.2 times greater than that of the other cases. This indicates that wave breaking for case $\gamma = 30°$ is significantly more intense and requires a longer time to reach stability. As shown in Fig. 13(c), the total gravitational potential energy decreases with increasing yaw angle. This is attributed to the intensified free-surface motion and increased entrained air, resulting in a reduction of effective water volume. Notably, for case $\gamma = 30°$, gravitational potential energy exhibits a brief fluctuation within $4 \leq t^* \leq 6$, corresponding to the fragmentation of the air tube observed in Fig. 6(e). In terms of total energy, shown in Fig. 13(a), the change in kinetic energy is dominant, and thus, the trend closely follows that of kinetic energy. All cases experience an initial decline in total energy, with greater yaw angles exhibiting more pronounced reductions, followed by a rapid increase and eventual stabilization. Interestingly, during the steady stage, the total energy for $\gamma = 10°$, $15°$, and $20°$ is slightly lower than that of the $\gamma = 0°$ case. This is primarily because the kinetic energies are nearly identical across these cases, while gravitational potential energy decreases more significantly with increasing yaw angle. However, due to the substantially higher kinetic energy in the $\gamma = 30°$ case, the total energy remains the highest, approximately 2.3–3.5 times that of the other cases. These variations in energy profiles suggest that intense bow wave breaking significantly increases the total energy of the fluid, particularly the kinetic component, which in turn contributes to increased hydrodynamic resistance on the ship hull.

B. Droplet characteristics

As observed in the primary evolution of free-surface breaking shown in Fig. 6, numerous splashing droplets are generated. Under strong wind conditions at sea, these droplets may become atomized into fine mist, potentially adhering to the windows of the ship's bridge and impairing visibility. Previous studies on wave breaking have largely overlooked this subtle yet practically significant flow phenomenon.[15,45,48] In the present work, the characteristics of droplet generation during bow wave breaking are analyzed.

Figure 14 presents the temporal evolution of droplet number and volume for various yaw conditions. In terms of droplet count, all cases exhibit a similar trend: an initial increase to a peak, followed by a decline and eventual stabilization. The number of droplets increases with yaw angle, with the $\gamma = 30°$ case producing significantly more droplets than the others. This indicates that free-surface breaking is much more intense under this condition, particularly due to the pronounced tearing of the liquid film at the wedge's leading edge, as
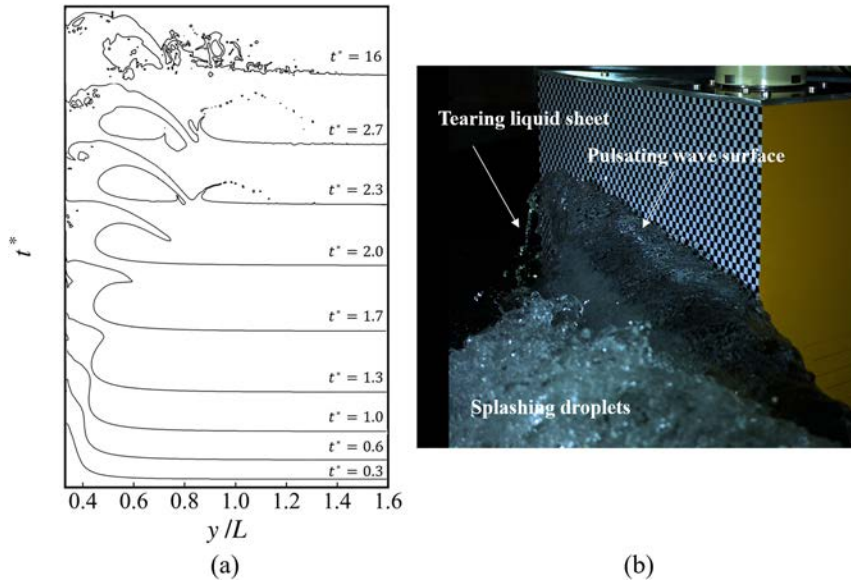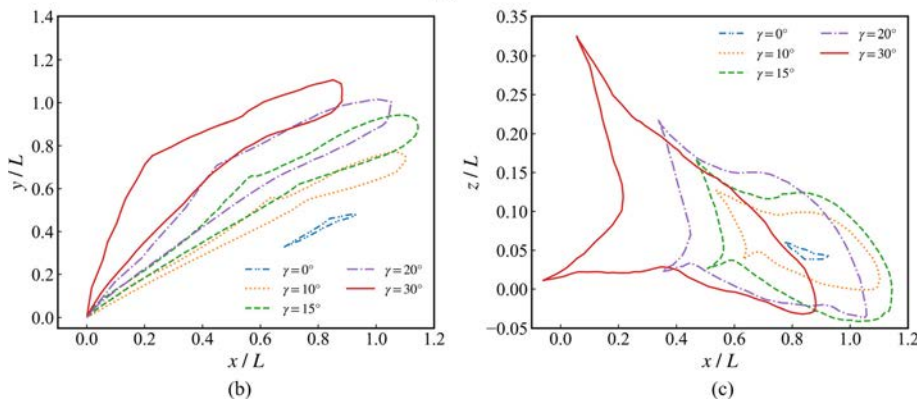
FIG. 10. The result of wave profile on the upstream-facing side. (a) The left is the time-history evolution of the cross section at $x/L = 0.35$ for case $\gamma = 30°$, and (b) the right is the experimental snapshot.
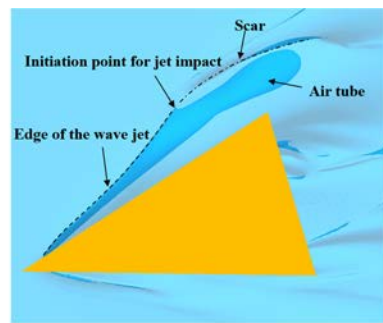

FIG. 11. Time-averaged distribution of the air tube. (a) Schematic diagram of the flow field around the air tube and its distribution in (b) the X–Y plane, and (c) the X–Z plane.

shown in Fig. 9. Figure 14(b) shows the evolution of total droplet volume, which generally follows the same trend as the droplet count. The main distinction lies in the appearance of a dip near the peak, characterized by a temporary decline followed by an increase. This feature is primarily attributed to the fragmentation of the air tube.

The droplet evolution for $\gamma = 30°$ case, based on high-resolution simulation results, is shown in Fig. 15. At $t^* = 2.3$, the droplets primarily form from the breakup of the splash jet generated when the plunging wave impacts the free surface. Numerous droplets are observed crashing into the free surface, causing indentations. At $t^* = 3$, due to the development of the air tube, the jet lifts, and smaller droplets form as a result of gravity-induced splitting. Referring to Fig. 14, at $t^* = 4.2$, both the number and volume of droplets reach their peak, with significant droplet fragmentation occurring near the
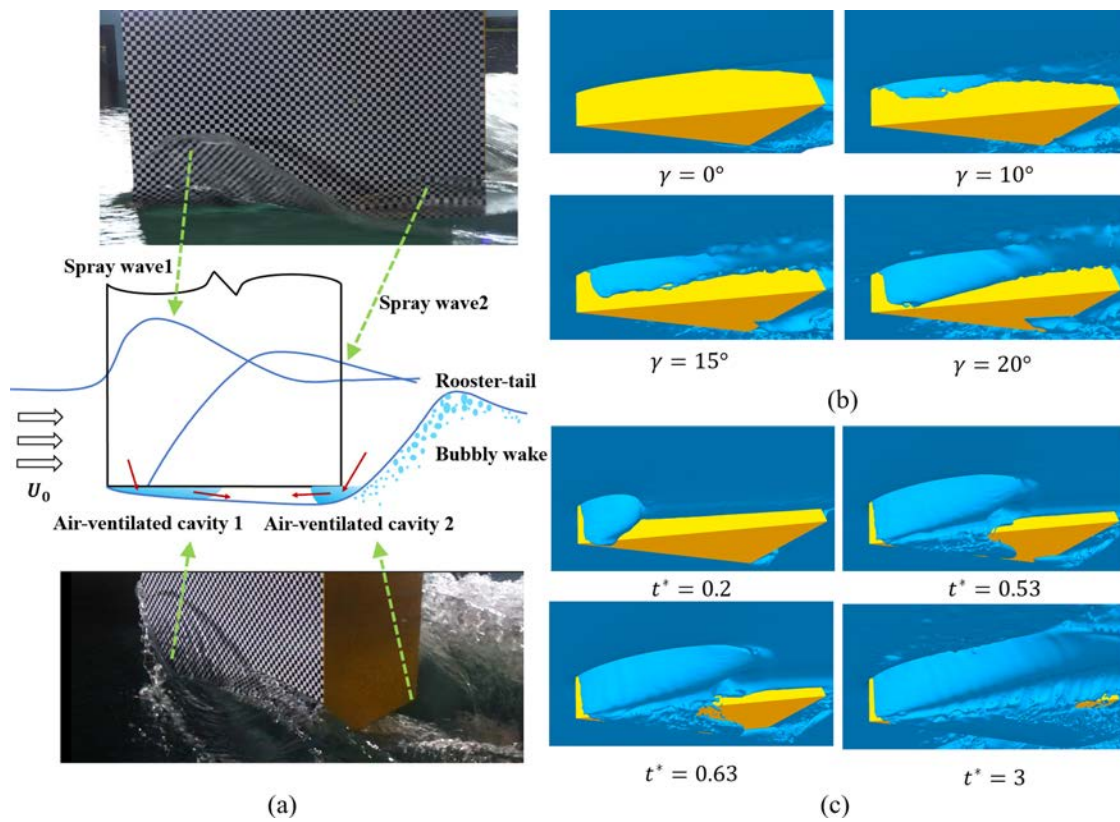
FIG. 12. Flow field results on the downstream-facing side about (a) the diagram of main structure, (b) the bottom view of the wedge at $t^* = 3$ for cases $\gamma = 0°, 10°, 15°,$ and $20°$, and (c) the bottom view of the wedge for case $\gamma = 30°$.

air tube and the jet. By $t^* = 8$, the droplet volume and number stabilize, mainly due to multiple breakups of the bow wave. From these time points, it seems that the droplet distribution is concentrated in specific regions. To observe the droplet aggregation, Fig. 16 presents the time-averaged number density distribution of droplets in a contour map. The higher the value, the greater the frequency of droplet occurrence. From the figure, it can be observed that droplets mainly accumulate in the region near the leading edge of the wedge-shaped bow, which is where the liquid film tears. They are also distributed along the edge where the plunging wave impacts the free surface. Additionally, a secondary distribution of droplets is seen splashing toward the inlet after they fall into the free surface. Moreover, some droplet aggregation is observed in the rooster-tail and scar regions.

Figure 17 shows the velocity distribution of droplets. In the X direction, the velocity magnitudes are relatively small, mainly concentrated below 0.2, which is dominated by the wave breaking in the stern and bow wave tail regions. A velocity distribution of $-0.2 \leq u_x/u_0 \leq 0$ can also be observed, which corresponds to the droplets splashing backward toward the inlet direction after falling onto the free surface in the bow wave region, as shown in Fig. 16. For the Y-direction velocity, after $t^* \geq 8$, the distribution becomes more uniform and is mainly concentrated in the range $0 \leq u_y/u_0 \leq 0.5$, which is generated by the multiple roll-ups of the wave jet on the upstream-facing side. A distinct velocity accumulation line at $u_y/u_0 = -0.3$ can be observed, which is primarily

caused by the spray wave on the downstream-facing side. For the Z-direction velocity, due to the effect of gravity, it is concentrated in the range $-0.5 \leq u_z/u_0 \leq 0$, with many droplets having very small velocities close to zero. In terms of total velocity, during the initial stage of wave breaking, the droplets' velocity is higher due to the influence of the Y-direction velocity. However, after $t^* \geq 8$, the total velocity stabilizes and is concentrated in the range $0.2 \leq u/u_0 \leq 0.8$.

Figure 18(a) shows the evolution of bubble size distribution for the $\gamma = 30°$ case. During the time period when the droplet number and volume reach their peak $2 \leq t^* \leq 6$, the droplet size distribution is primarily below 10 mm. After $t^* \geq 8$, the evolution stabilizes, and the number of larger droplets decreases, with the equivalent droplet radius concentrating below 7 mm. Figure 18(b) presents the droplet size spectra for different yaw conditions. Overall, in the region where the equivalent radius $r_{eff} \geq 5$ mm, the size distribution follows a power law with an exponent of -4.5. This finding is in agreement with the dimensional analysis results of Deane and Stokes,[44] which indicate that $N(r) \propto (\sigma/\rho_w)^{0.5} r^{-4.5}$, as well as the numerical results.[26] It is worth mentioning that for these splash droplets and sprays, despite the differing formation mechanisms, such as sea spray spume drops caused by strong winds, pure wave breaking, or bubble bursting, the number of droplets of the same size follows similar power-law relationships.[45,48] The observed -4.5 power law in droplet size distribution, suggests a fundamental scaling mechanism, where abundant fine droplets may
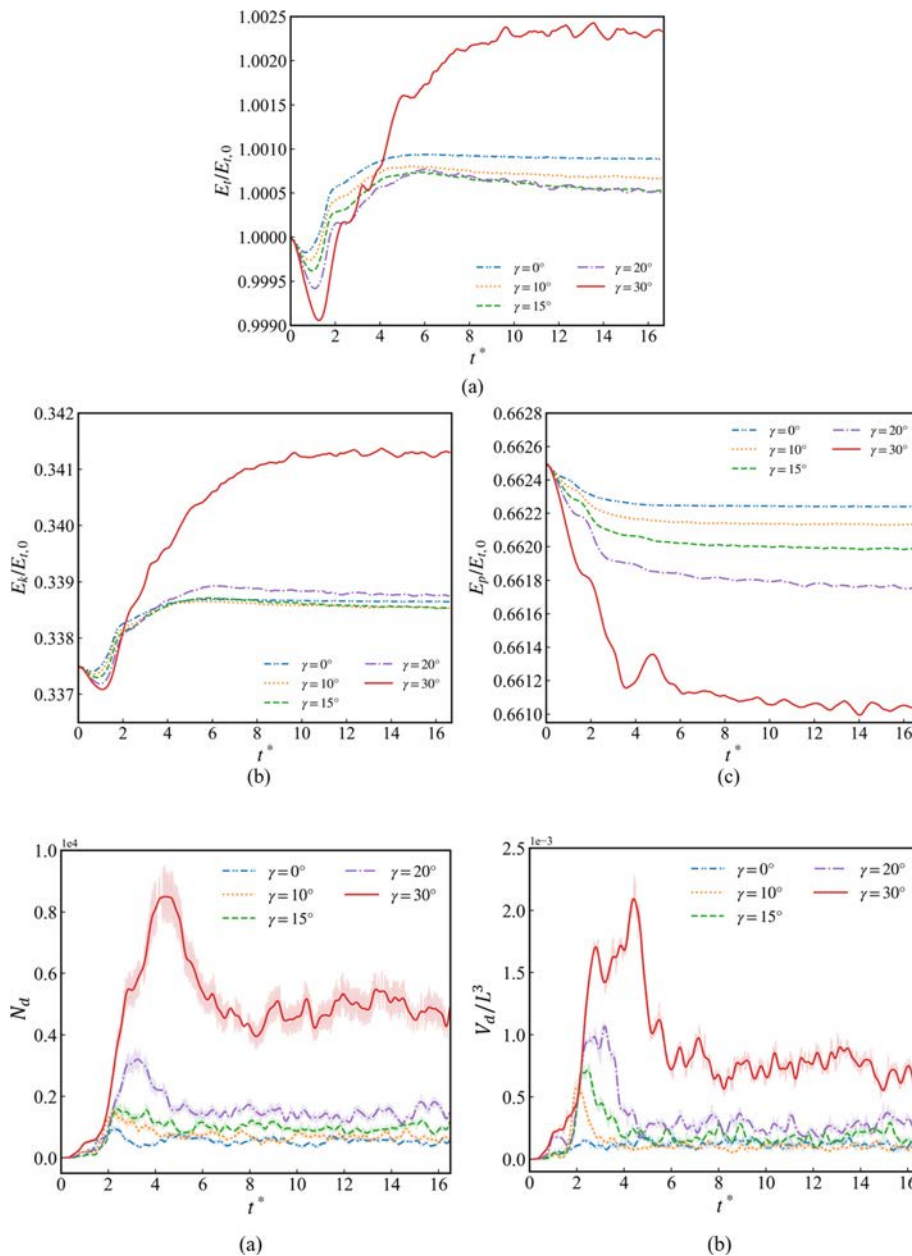
FIG. 13. The curves of water body energy budget over time for (a) total energy, (b) kinetic energy, and (c) potential energy. All energy values are normalized by the initial total energy.

FIG. 14. The curve of droplet characteristics. Time history of (a) the droplet number and (b) the droplet volume.

affect radar and optical sensors, while large droplets can form spray curtains that obstruct bridge visibility under rough sea conditions.[72]

C. Entrained air structures

An important feature of wave breaking is the entrainment of large amounts of air into the water, accompanied by the formation of numerous whitecaps on the free surface. The term "entrained air structures" refers to all enclosed air structures that are entrapped within the water and disconnected from the atmosphere. These entrained air structures typically exhibit a wide range of size distributions. Figure 19

shows the time-averaged volume fraction results in a transverse cross section for different yaw conditions, where the free surface is extracted from the time-averaged results. For the $\gamma = 0°$ case, the bow wave does not undergo significant plunging breaking, and the entrained air is distributed on both sides of the wake. For this case, the rooster-tail expands and rolls outward as it moves away from the ship. For larger yaw angles, the direction of the rooster-tail wave changes, and it begins to roll toward the upstream-facing side, as shown in Fig. 19(e), rather than dispersing symmetrically to both sides. This phenomenon is closely related to the air-ventilated at the bottom of the wedge-shaped bow, which causes the wake produced by the flat stern to lose its
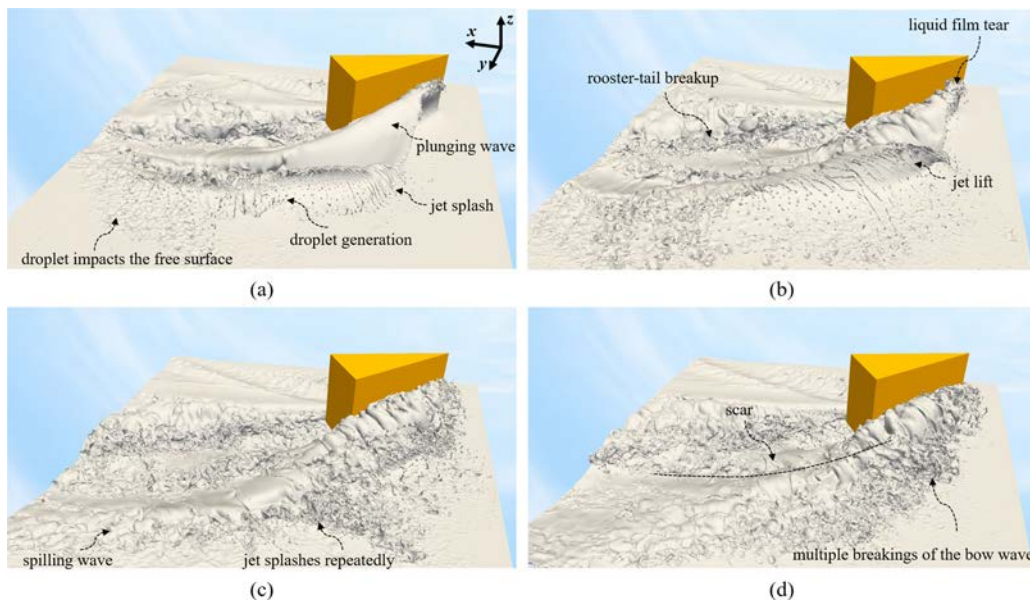
FIG. 15. Evolution of droplets above the free surface for case $\gamma = 30°$. (a) $t^* = 2.3$, (b) $t^* = 3.0$, (c) $t^* = 4.2$, and (d) $t^* = 8$.
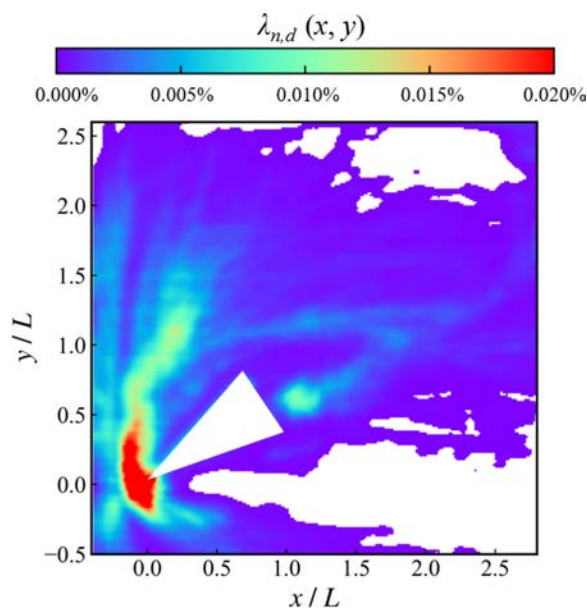

**FIG. 16.** Time-averaged distribution of droplet number density for case $\gamma = 30°$.

symmetry. As a result, more air is entrained in the wake compared to the $\gamma = 0°$ condition. Additionally, a notable feature is the presence of the air tube entrained by the bow wave at different yaw angles. The distribution of these air tube under different conditions has been analyzed in Fig. 11. From Fig. 19, it can be observed that in the downstream flow direction behind the air tube, the air accumulation region still exists. This indicates that the air tube is not stable but instead

continuously break apart and regenerate, thus constantly introducing air into the water. Finally, the air entrained by the stern and bow waves will mix downstream, away from the wedge.

Furthermore, the time-averaged volume and number of entrained air structures of various sizes are extracted, as shown in Fig. 20. In the X-direction, the number of entrained air structures consistently increases across all yaw conditions. For $\gamma = 0°$, $10°$, $15°$, and $20°$, the air volume increases until it reaches a peak, then decreases and stabilizes. The higher the yaw angle, the higher the peak value. This is mainly due to the continuous fragmentation of larger air structures into smaller ones or their escape through the free surface. As a result, the overall number of air structures increases, but only small-size air structures that can persist exist in the wake region far from the wedge, leading to stabilization in the longitudinal direction. For $\gamma = 30°$ case, due to more intense bow wave breaking, a longer longitudinal range is required. As a result, the X direction does not show stabilization within the current computational domain. In the Y-axis direction, the distribution of the number and volume of entrained air structures is similar. For $\gamma = 0°$, the distribution is symmetric. For yaw conditions, however, the entrained air is mainly distributed along the positive Y axis and exhibits two distinct peaks. From Fig. 19, it is evident that the larger peak corresponds to the mixed region behind the flat stern and air tube, while the smaller peak represents the diffusion region of the bow wave. In the Z direction, the volume and number of entrained air structures show a similar trend, increasing to a peak and then decreasing. The higher the yaw angle, the deeper the distribution of entrained air structures. Additionally, both the peak number and volume of entrained air structures are greater for higher yaw angles.

To make the distribution of air structures more obvious, the instantaneous air structures for $\gamma = 30°$ case are visualized as spheres with equivalent radius, as shown in Fig. 21. At $t^* = 1.3$, only a small number of air structures are entrained by the flat stern. At $t^* = 2.6$, the bow wave has formed the air tube, and the tail of the air tube entrains
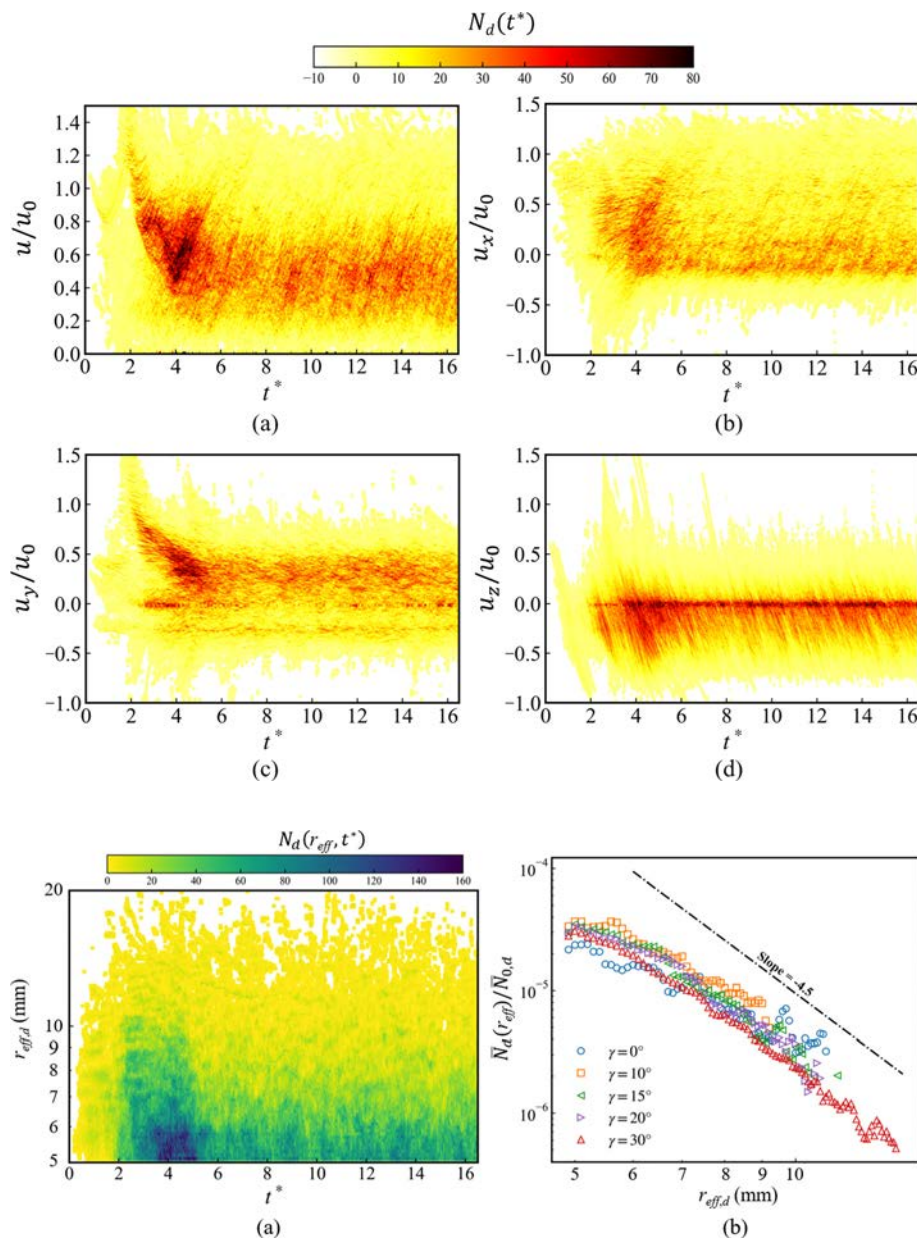
FIG. 17. Contours of droplet velocity for case $\gamma = 30°$. The time evolution of the droplet velocity includes (a) the total magnitude distribution, (b) the velocity in X-axis direction, (c) the velocity in Y-axis direction, and (d) the velocity in Z-axis direction.
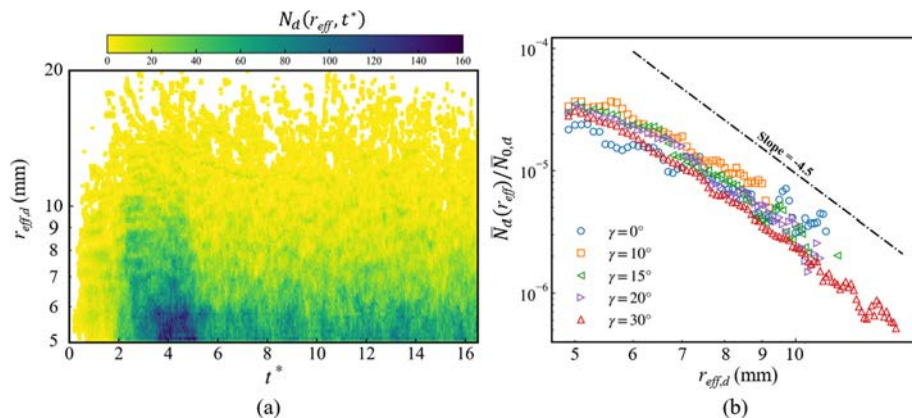
FIG. 18. The characteristics of droplet size include (a) the time history evolution of droplet size for case $\gamma = 30°$ and (b) the time-averaged droplet size distribution.

some air structures. At $t^* = 4$, a large number of air structures can clearly be seen at the tail of the air tube. By $t^* = 16$, the air tube has fully developed, with a significant presence of small-scale air structures. At different instantaneous moments, air structures of various sizes can be observed, and there is a considerable size difference between them.

Generally, gas structures in water are categorized as bubbles if their radius ranges from a few micrometers to a few millimeters, and air cavities if their radius ranges from a few millimeters to a few meters. For clarity, an equivalent radius of 15 mm is used as the boundary in this study, with structures larger than 15 mm classified as air cavities and those smaller than 15 mm as bubbles. The bar chart in Fig. 22 shows the time-averaged percentage of bubbles and cavities in the total

air structures. It is evident that the number of air cavities is very small, accounting for less than 5%, while the volume proportion of air cavities even reaches up to 60%. Air cavities are fewer and exist for shorter periods in the water, having minimal impact on the overall flow field. Therefore, when analyzing the statistical characteristics of bubbles, air cavities should be excluded. This distinction, while often overlooked in some large-scale wave-breaking numerical studies,[27,32,50,69] is emphasized in experimental studies.[44,73–75]

D. Characteristics of bubble flows

The bubble flow in the wake of the ship, which persists for a long time during the ship's navigation, is a significant feature of wave
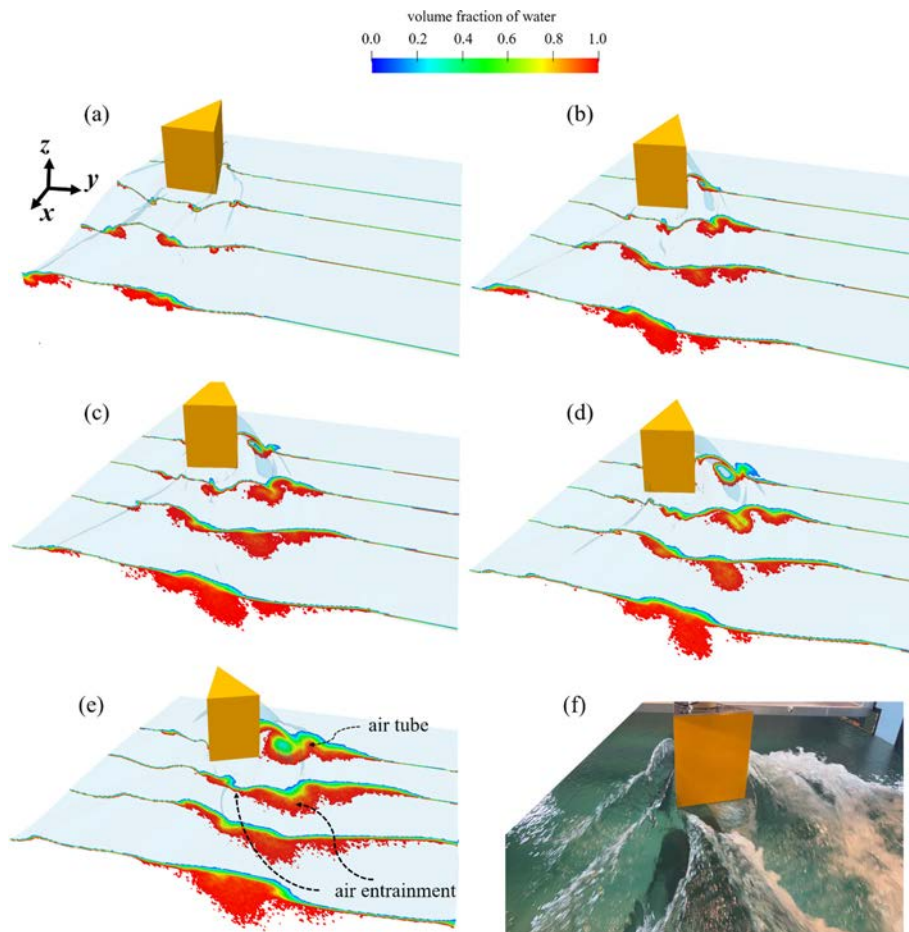
FIG. 19. Time-averaged void fraction of water. The blue iso-surface is generated by the averaged volume fraction of 0.5, for the different yaw angles (a) $\gamma = 0°$, (b) $\gamma = 10°$, (c) $\gamma = 15°$, (d) $\gamma = 20°$, (e) $\gamma = 30°$, and (f) experimental snapshot.

breaking. Figure 23 shows four instantaneous results of bubble flow development in the water for $\gamma = 30°$ case. At $t^* = 1.6$, a few bubbles have been generated at the stern. At $t^* = 3.0$, the formation of an air tube at the bow is clearly visible, and the air tube is rotating and breaking into numerous small bubbles. At $t^* = 4.8$, four distinct bubble flows can be observed: bubble flow I is formed by secondary splashing due to wave roll-up, bubble flow II results from the breakup of the air tube, bubble flow III is formed by the rooster-tail wave from the stern, and bubble flow IV is created by the spray wave on the downstream-facing side. By $t^* = 16$, the bow wave breaking has reached a quasi-steady state. Compared to $t^* = 4.8$, the air tube has fully developed, and the position of bubble flow I has moved forward. This is mainly due to the continued multiple splashing events from the initial plunging wave at the bow, which continually entrains bubbles. Furthermore, bubble flow II and III mix in the wake, while bubble flow I spreads within the wake. These snapshots highlight the dynamic and evolving nature of bubble flow, which interacts with the wedge and surrounding fluid. Different sources contribute to the formation of bubble structure and its subsequent mixing and diffusion.

Figures 24 and 25 show the distribution of bubbles in the X–Y and X–Z planes for each yaw angle condition. A notable difference in the bubble distribution across the yaw conditions is observed on the upstream-facing side. For small yaw angles, bubbles are concentrated behind the wedge-shaped bow, while for larger yaw angles, bubbles are distributed over a wider range. In the X–Y plane, comparing the bubble number density, it can be seen that the symmetric bubble distribution path, caused by the rooster-tail, gradually disappears. For $\gamma = 30°$ case, the bubble wake flow on the left side of the stern has completely disappeared. For $\gamma = 10°$, $15°$, and $20°$ cases, it is clear that in addition to the first path of bubbles induced by the plunging wave, a second path of bubbles, similar to bubble flow I seen in Fig. 23(c), can also be observed. Furthermore, all yaw conditions exhibit mixing of the bubble flows in the wake. In the X–Z plane, the bubble distribution depth increases with the yaw angle. The bubble number density shows two distinct bubble paths generated by the bow wave breaking and stern wave breaking. The wake bubbles move from the stern's bottom toward the free surface, while the bubbles from the bow wave exhibit a clear downward sweeping behavior.

Figure 26(a) presents the temporal evolution of the total volume of entrained bubbles for each yaw angle condition. All conditions exhibit a similar trend, with the bubble volume continually increasing and eventually stabilizing. Additionally, the total volume of bubbles increases with the yaw angle. Further analysis of the volume curves' power spectral densities (PSD) is shown in Fig. 26(b). It can be observed that the PSD for several conditions exhibit a -2 power-law distribution. This is primarily because the bubbles are generated and
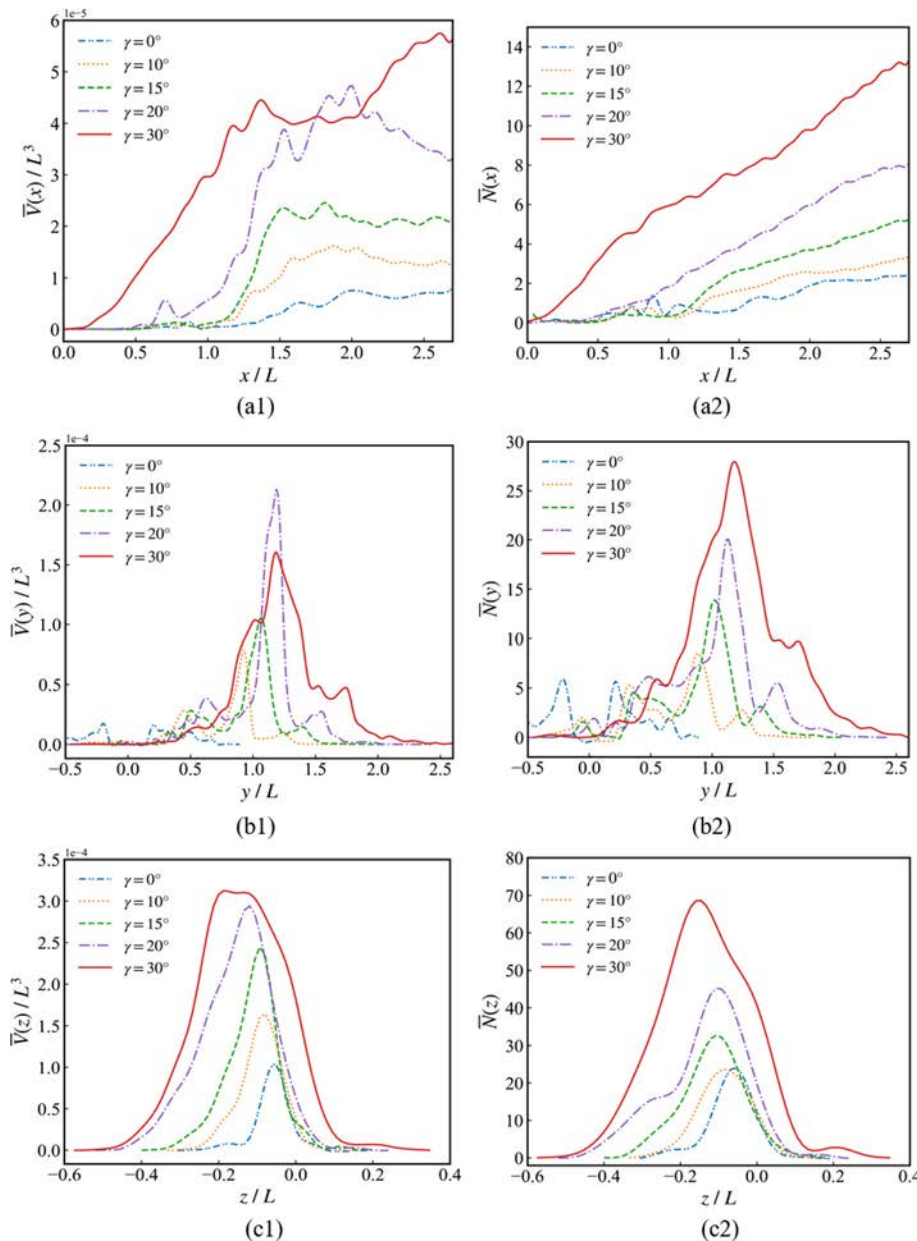
FIG. 20. Spatial distribution of entrained air structures including enclosed air structures of various sizes in water. Volume and number distributions in (a1) and (a2) X-axis direction, (b1) and (b2) Y-axis direction, and (c1) and (c2) Z-axis direction.

evolve along the free surface, influenced by turbulent dissipation near the surface. Due to the obstruction of the free surface, turbulence near the surface tends to take on a quasi-two-dimensional state, causing the bubble volume's power spectral density to display high-frequency decay with a slope of approximately -2.[27] This finding aligns with the work of Metcalf et al.,[76] who noted that unsteady responses, such as wave height, turbulence intensity, surface velocity, and vorticity on the free surface, exhibit -2 power-law spectral density behavior.

Numerous experiments[73–76] and numerical simulations[45–48] have confirmed that the bubble size distribution generated by pure wave-breaking phenomena follows a power-law distribution. For bubbles smaller than the Hinze scale, surface tension-induced flow instabilities dominate, with a density exponent of -1.5. For bubbles larger than the Hinze scale, shear forces[77] in the fluid dominate, leading to a density exponent of $-10/3$. Figure 27 shows the bubble size spectrum for different yaw conditions. As the bubble radius increases, the power-law exponent gradually deviates from $-10/3$ and approaches -4.5 in this study. This suggests that the presence of the wedge-shaped bow reduces the number of large bubbles. On the one hand, large bubbles in the wake of the wedge are more easily detached from the vortex entrainment mechanisms caused by wave breaking due to buoyancy. On the other hand, the wedge-shaped bow generates complex separation vortices that may enhance the shearing of large bubbles, potentially contributing to a reduction in their residence time underwater.
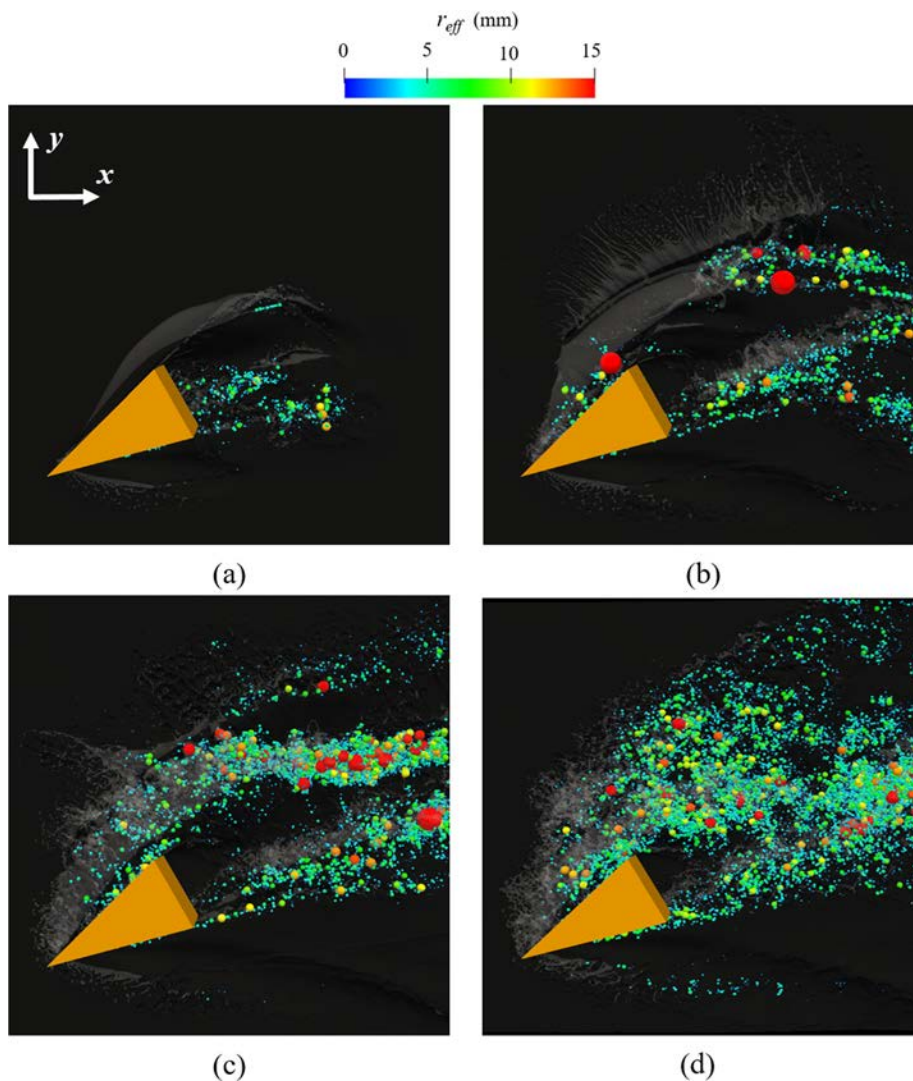
FIG. 21. Instantaneous entrained air structures distribution for case $\gamma = 30°$ at (a) $t^* = 1.3$, (b) $t^* = 2.6$, (c) $t^* = 4.0$, and (d) $t^* = 16$.

These two factors contribute to the reduction in the number of large bubbles and a shift in the power-law exponent toward -4.5. This distribution behavior is similar to phenomena observed in numerical studies of bubble wake flows behind the high-speed stern ship[50,69] and the hydrofoil.[27,56]

The vortex structures at the bow are closely linked to the free-surface breaking mechanisms. Bubbles are generated due to the movement of flow field structures, which cause free-surface breaking and entrainment. By analyzing the vortex structures, we can observe the complex flow dynamics that contribute to this process. The instantaneous vortex structure for $\gamma = 30°$ case is shown in Fig. 28. The vortex structure with the largest coverage is the primary vortex generated by the first wave breaking and subsequent rolling at the bow. This vortex extends from the bow to the stern, perfectly overlapping with the path of bubble flow II shown in Fig. 23, further confirming that the dynamic motion of the bubbles is influenced by the vortex structures. Since bubble flow II is caused by the rotational breaking of the air tube structure,

we can observe the transverse rotational movement of the primary vortex. Additionally, after the first roll at the wedge-shaped bow, secondary and sub-secondary vortex structures are formed due to subsequent free-surface chaotic breaking. These vortices dissipate as the bubbles rise and disappear, without extending all the way to the stern. When examining the intensity of the vortex structures formed during the bow wave breaking, we find that the strongest vortices are concentrated on the upstream-facing side of the wedge, where the most intense nonlinear breaking occurs on the free surface. Furthermore, we can observe the tip vortex that extends from the leading edge of the wedge, which contributes to the formation of the air-ventilated cavity at the bottom of the wedge. The tip vortex stretches all the way to the stern, where it mixes with the rooster-tail vortex structure, further enhancing the bubble entrainment phenomenon at the stern. This intricate interplay between the vortex structures and bubble dynamics highlights the critical role that vortex motion plays in the overall wave breaking and air entrainment processes around the ship. The
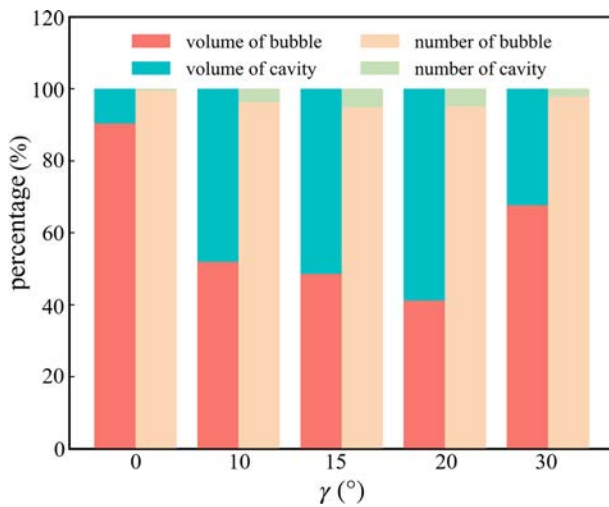
FIG. 22. The percentage of the volume and number of bubbles and cavities in the entrained air structures.

streamwise vorticity of the water body, averaged along the vertical (depth) direction, is shown in Fig. 29. The results reveal that the trajectory of bubble distribution closely overlaps with regions of high vorticity, indicating that bubble motion is strongly influenced by the combined effect of multiple vortices. The primary vortex entrains a concentrated bubble region, which merges with the rooster-tail vortex downstream, resulting in a densely populated bubble zone in the wake. The interaction between the tip vortex and the rooster-tail vortex is clearly observed on the downstream-facing side, where bubbles accumulate within regions of peak vorticity. In contrast, the secondary and sub-secondary vortices generate fewer bubbles, with more scattered distributions and no significant mixing in the wake.

V. CONCLUSIONS

Building on the previous experiment,[1] high-fidelity numerical simulations are employed in this study to investigate the bow wave-breaking phenomena of a wedge-shaped bow at various yaw angles, aiming to analyze small-scale flow structures that are difficult to observe and measure experimentally. The results indicate that yaw angle significantly influences the wave-breaking process, particularly the evolution of the free surface and the behavior of small-scale structures such as bubbles and droplets. The main conclusions of this study are as follows:

As the yaw angle increases, the wave elevation on the upstream-facing side of the wedge-shaped bow significantly increases, leading to more intense liquid film tearing and more violent plunging wave breaking. The distribution angle of the initial segment of the air tube formed by the bow wave rolling expands, and the initial impact point shifts forward. As γ increases from $0°$ to $30°$, the streamwise angle gradually increases from $19.7°$ to $28.1°$, while the sweep-down angle increases
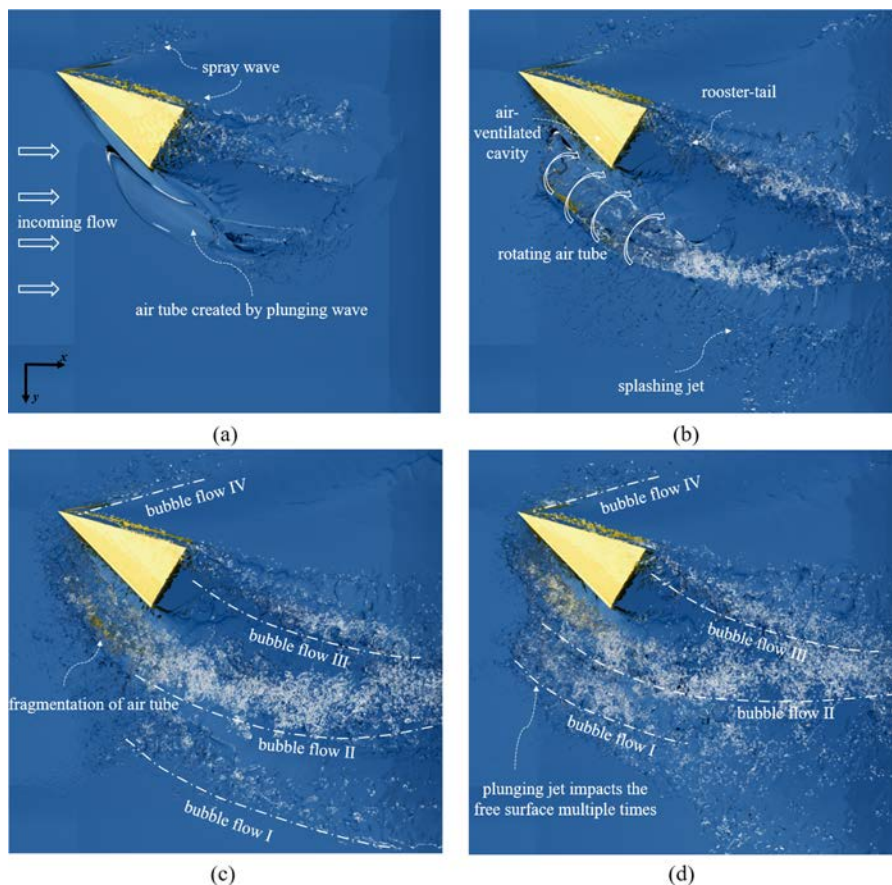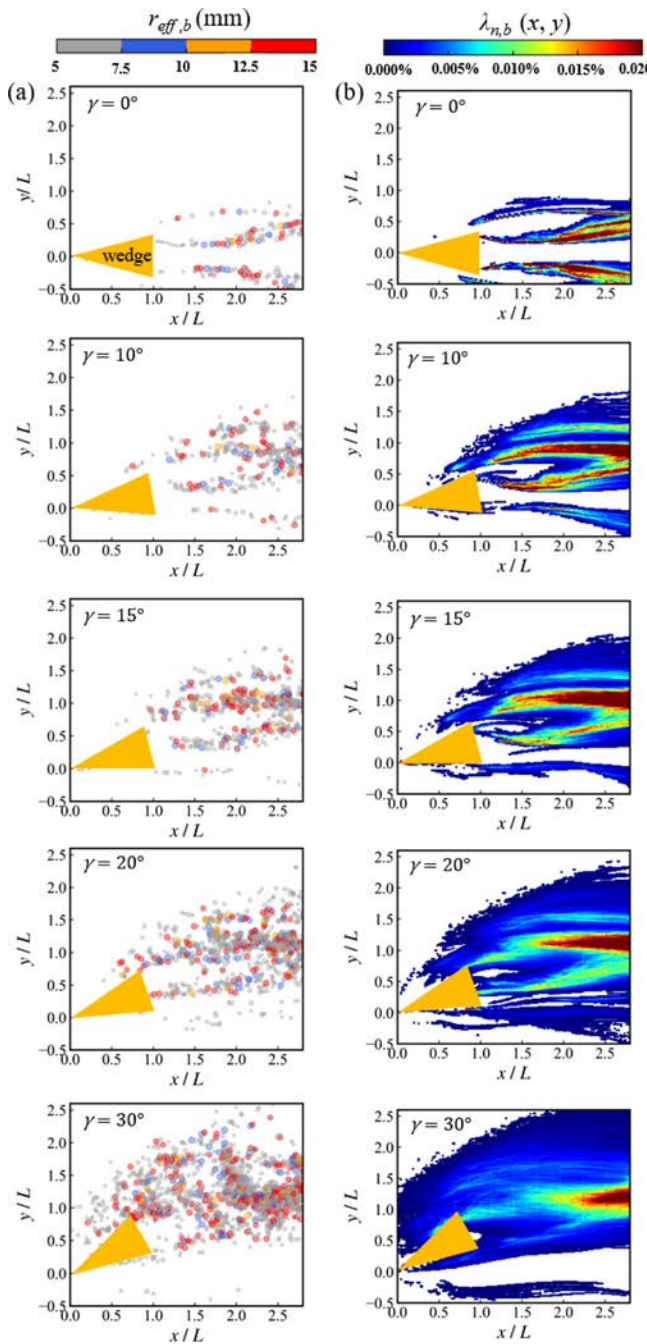

FIG. 23. The development of bubble flow for case $\gamma = 30°$ at (a) $t^* = 1.6$, (b) $t^* = 3.0$, (c) $t^* = 4.8$, and (d) $t^* = 16$.
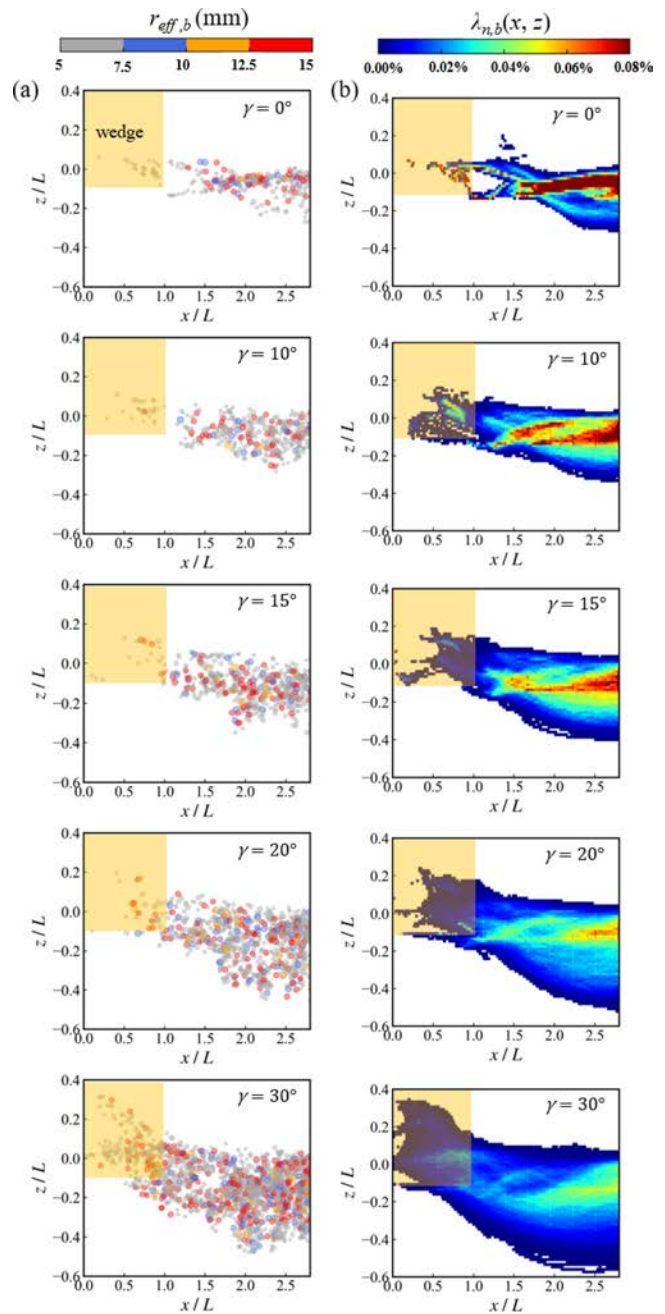
FIG. 24. Spatial distribution of bubbles in the X–Y plane. (a) The instantaneous results with equivalent radius and (b) the time-averaged number density distribution.

FIG. 25. Spatial distribution of bubbles in the X–Z plane. (a) The instantaneous results with equivalent radius and (b) the time-averaged number density distribution.

from 9.6° to 27.3°, indicating that the air tube becomes more inclined both horizontally and vertically under stronger yaw conditions.

On the downstream-facing side of the wedge, the spray waves and a deep concave free surface are observed. The air-ventilated cavity structure forms at the bottom of the wedge, accompanied by distortion of the rooster-tail wave morphology in the wake. For $\gamma = 30°$ case,

four distinct water–air–bubble mixed flow paths are formed on the free surface, and energy analysis reveals that the total energy consumption increases by approximately 2.3–3.5 times compared to the other yaw condition, significantly enhancing the nonlinear effects on the free surface.

Droplets primarily form during the process of bow wave impacting the free surface. Their number and volume show a significant
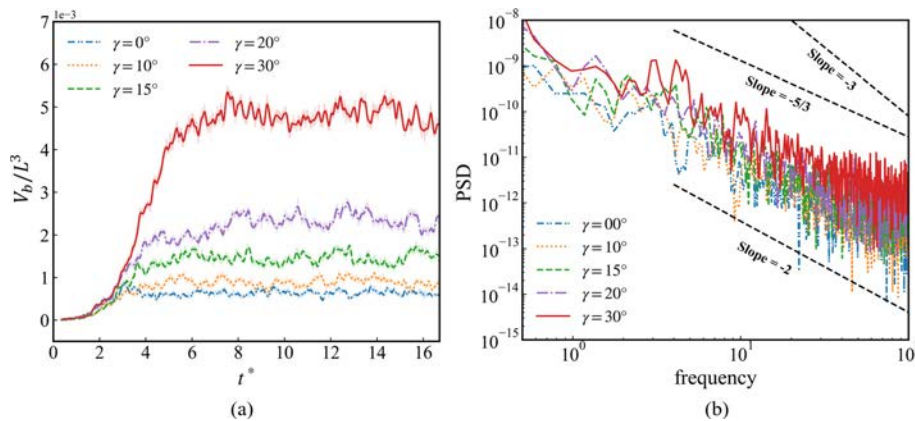
23 July 2025 00:17:37

FIG. 26. Time characteristics of bubble volume for (a) time evolution, and (b) power-spectral densities.
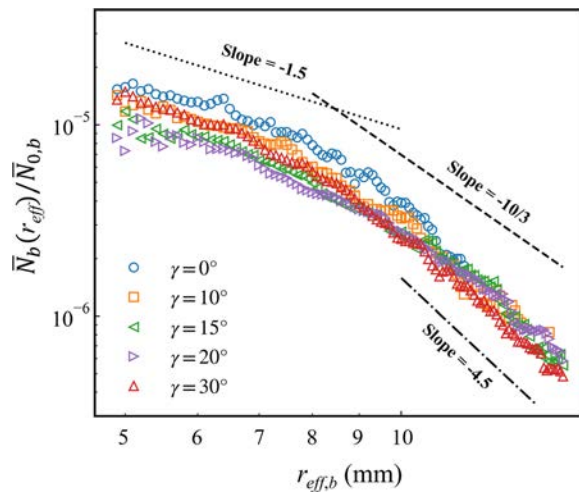

FIG. 27. Time-averaged bubble size distribution.

increase with yaw angle. At high yaw angles, droplet distribution is concentrated in the bow wave-breaking zone and along the secondary splashing path. In addition, the droplet size spectrum follows a power law with an exponent of -4.5 in terms of equivalent radius.

The entrained air is mainly influenced by the breaking of the bow wave and stern wake, with mixing observed at the stern. This study finds that air cavities with an equivalent radius greater than 15 mm account for up to 60% of the volume, although their number is less than 5%. This emphasizes the need to distinguish between bubbles and enclosed air cavity structures when analyzing entrained air structures in large-scale wave-breaking studies.

An analysis of bubble spatial distribution reveals clear sweep-down motion of bubbles generated by bow wave breaking. As the yaw angle increases, the vertical penetration depth of the bubbles increases, and the asymmetry of bubble paths in the rooster-tail wave becomes more pronounced. With increasing bubble size, the size spectrum transitions from a $-10/3$ to -4.5 power law, suggesting that the wedge-shaped bow may disturb the flow field in a manner that promotes large bubble fragmentation and potentially shortens their residence time underwater.[27,69] Moreover, bubble distribution is influenced by the
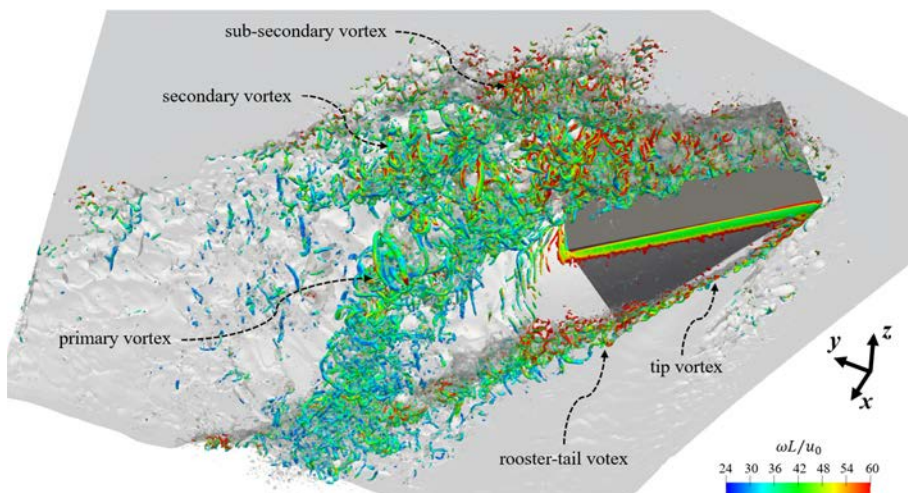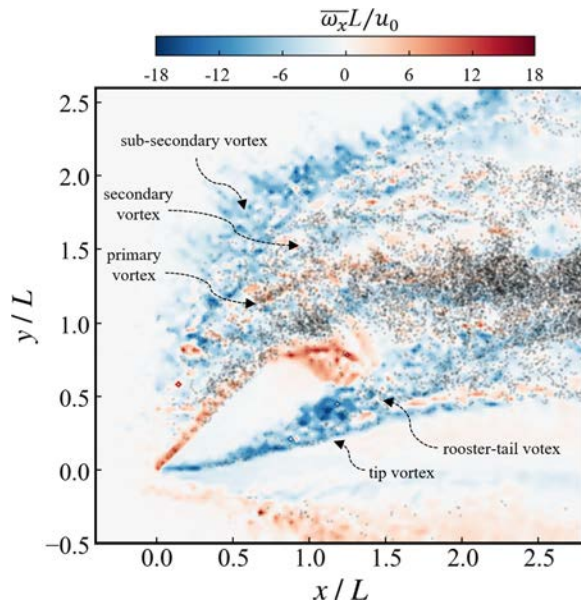
FIG. 28. The three-dimensional turbulent vortex structures underwater for case $\gamma = 30°$ at $t^* = 16$. Iso-surface of vortex is extracted via contour Q-criterion = 1500 s^{-2} and colored via vorticity.

FIG. 29. Streamwise vorticity of the water phase for case $\gamma = 30°$ at $t^* = 16$, averaged in the vertical direction. The black dots represent the instantaneous locations of bubbles, highlighting their correlation with vortical structures.

synergistic effect of the primarily vortex, tip vortex, and rooster-tail vortex, with the primarily vortex dominating the transport path of bubble flow II, and the mixing of the tip vortex and rooster-tail vortex intensifying bubble entrainment in the wake.

This study provides a detailed understanding of how yaw angle influences the water–air–bubble multiphase dynamics in bow wave breaking, offering new insights into drag reduction, spray suppression, and bubble wake prediction.[72] The predicted bubble sweep-down distribution may inform sonar array placement, while the estimated air volume fraction in the wake can support studies on cavitation and propulsion under aerated conditions. These findings also offer potential guidance for ship maneuvering and stealth design. Future work may incorporate experimental validation of small-scale statistics and explore the correlation between vortex strength and bubble behavior, as well as extend the analysis to more complex hull forms and multiphysics scenarios.

ACKNOWLEDGMENTS

AUTHOR DECLARATIONS
Conflict of Interest

The authors have no conflicts to disclose.

Author Contributions

Yuming Shao: Data curation (equal); Formal analysis (equal); Investigation (equal); Methodology (equal); Validation (equal); Visualization (equal); Writing – original draft (equal). **Bowei Song:** Project administration (equal); Resources (equal). **Jianhua Wang:** Conceptualization (equal); Funding acquisition (equal); Investigation (equal); Methodology (equal); Project administration (equal); Supervision (equal); Writing – review & editing (equal). **Wentao Wang:** Methodology (equal); Project administration (equal). **Decheng Wan:** Conceptualization (equal); Resources (equal); Software (equal); Supervision (equal).

DATA AVAILABILITY

The data that support the findings of this study are available from the corresponding author upon reasonable request.

APPENDIX: SUPPLEMENTARY ANALYSIS OF INFLUENCES ON SMALL-SCALE STRUCTURES

1. Bubble–droplet identification method

In the study of bow wave breaking, numerous multi-scale flow structures, such as bubbles and droplets, can be observed. To effectively analyze these small-scale structures, it is essential to accurately identify each droplet or bubble during the computational process. This study utilizes the tag function from the Basilisk flow solver.[48,51] The underlying principle of this method is based on the flood-fill algorithm used in image recognition.[32] Starting from a seed point within a single connected region, the algorithm marks all grid points within the computational domain according to selected criterion.

Take bubble recognition as an example. In this research, bubble identification is performed using the volume fraction of water-based tagging method. Initially, the grid cells are tagged to identify the neighborhood of each bubble. Specifically, each cell is assigned a unique tag based on its connectivity with neighboring cells, and the tagging process employs multigrid techniques to ensure accurate transfer and update of tag values. This iterative method progressively merges the tags of neighboring cells until all connected cells belong to the same neighborhood. Subsequently, to reduce the range of tag values, sorting and deduplication are applied, compressing the tag values into unique indices that represent different bubble neighborhoods. This approach efficiently identifies bubbles of varying sizes and can accurately track the dynamic evolution of bubbles under complex flow conditions. Additionally, relevant physical quantities of each bubble, such as volume (v_{id}), centroid ($\mathbf{x}_{id}$), and velocity ($\mathbf{u}_{id}$), are computed.

$$v_{id} = \sum_{\text{tag}_{id}=1} (1 - f_i) V_i, \tag{A1}$$

$$\mathbf{x}_{id} = \frac{1}{v_{id}} \sum_{\text{tag}_{id}=1} (1 - f_i) \mathbf{x}_i V_i, \tag{A2}$$

$$\mathbf{u}_{id} = \frac{1}{v_{id}} \sum_{\text{tag}_{id}=1} (1 - f_i) \mathbf{u}_i V_i, \tag{A3}$$

where f_i, V_i, $\mathbf{x}_i$, and $\mathbf{u}_i$ represent the volume fraction, geometric volume, centroid coordinates, and velocity of the grid cell i, respectively. Furthermore, the above approach can be easily adapted to identify droplets with only minor modifications.
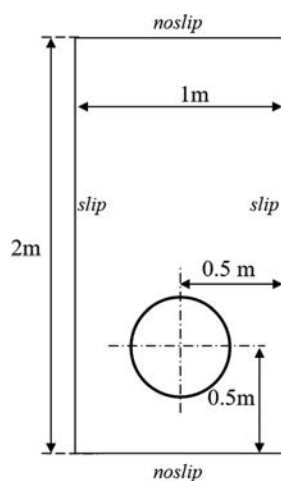
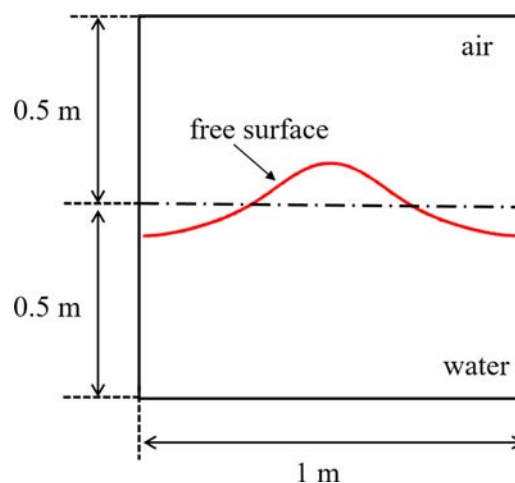FIG. 30. Computational domain setup for the bubble rising case.

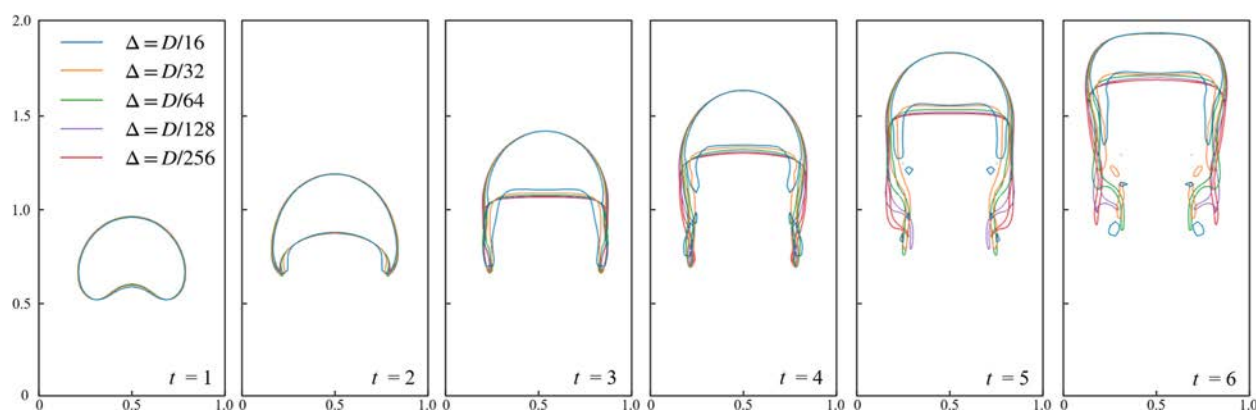FIG. 33. Computational domain setup for the Stokes wave-breaking case.

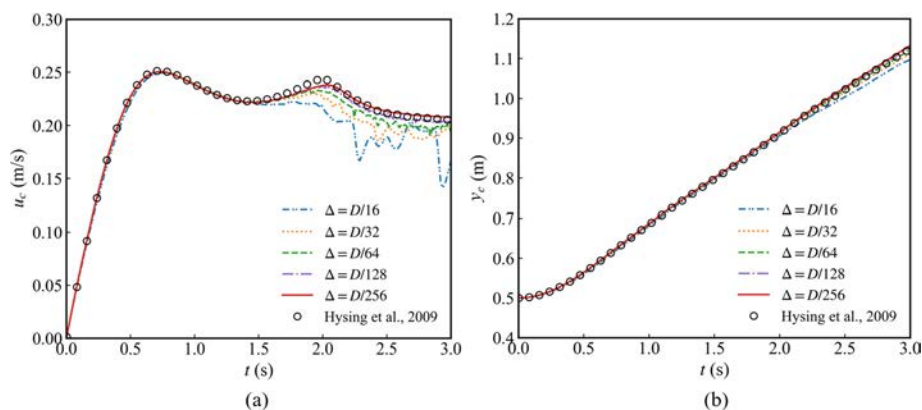FIG. 31. Evolution of bubble shape at different grid resolutions.

FIG. 32. Time-history curves under different grid resolutions: (a) rising velocity of the bubble and (b) vertical position of the bubble centroid.
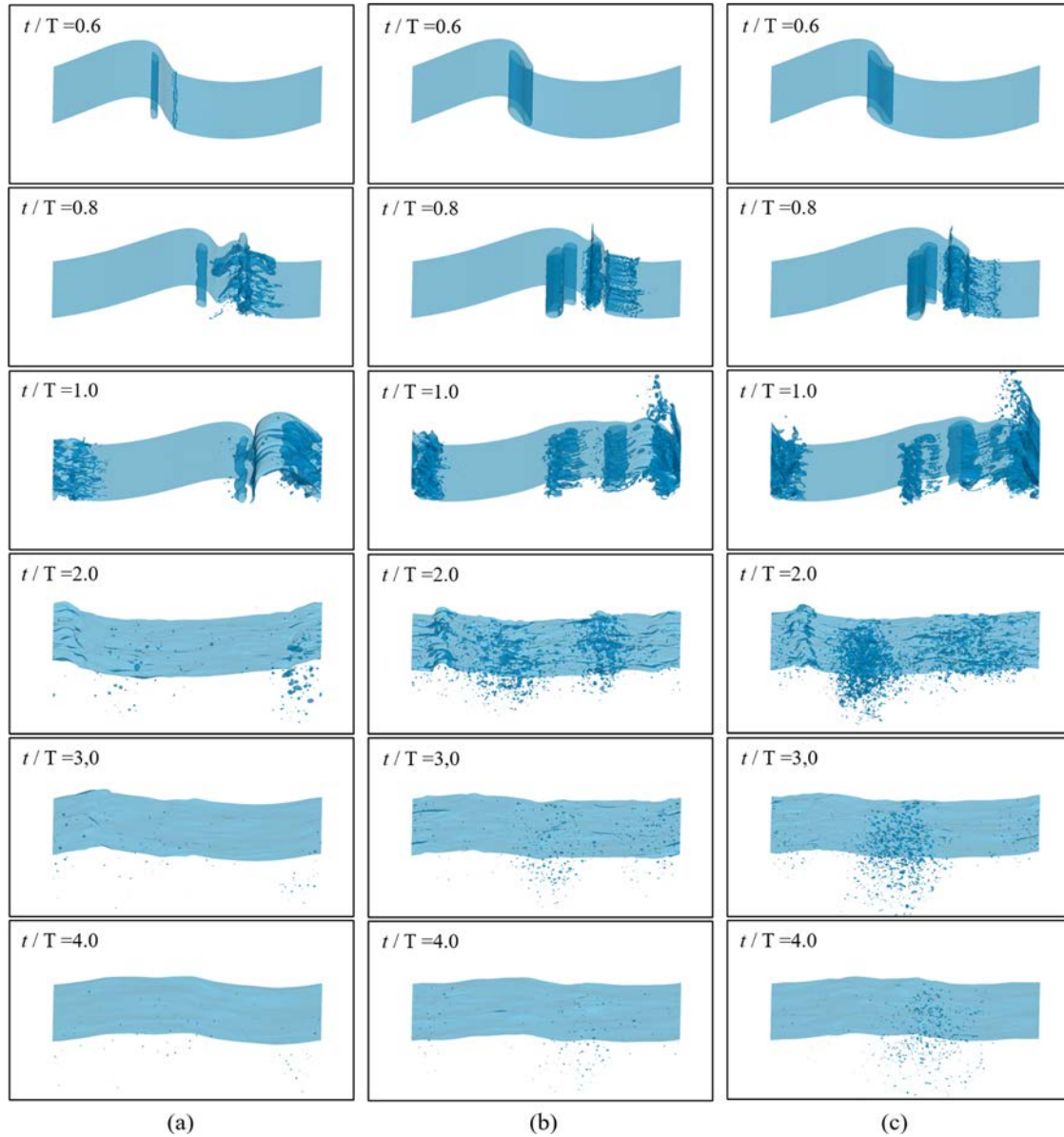
23 July 2025 00:17:37

FIG. 34. Instantaneous free-surface snapshots under different surface tension conditions: (a) $Bo = 200$, (b) $Bo = 1000$, and (c) $Bo = 2000$.

2. Rising bubble

The two-dimensional rising bubble is one of the benchmark cases for two-phase flow simulations.[78] Under the influence of gravity, the bubble undergoes significant deformation during its ascent. As shown in Fig. 30, a bubble with a diameter of $D = 0.5$ m is initialized in a computational domain measuring 1 m in width and 2 m in height. Slip boundary conditions are applied on the lateral boundaries, while no-slip conditions are imposed at the top and bottom. The density and viscosity ratios between the surrounding fluid and the bubble are set to $\rho_1/\rho_2 = 1000$ and $\mu_1/\mu_2 = 100$, respectively,

corresponding to a Reynolds number of $Re = \rho_1 g^{1/2} D^{3/2}/\mu_1 = 35$. Simulations are performed using five grid resolutions: $\Delta = D/16$, D/32, D/64, D/128, and D/256, which correspond to grid spacings of 31.3, 15.6, 7.8, 3.9, and 2.0 mm, respectively.

Figure 31 presents the evolution of the bubble shape during the rising process. Significant deformation is observed, with the bubble transforming from an initially circular shape into an irregular form characterized by trailing filaments on both sides. The primary differences across grid resolutions are found in the representation of these skirt-like structures. For high-resolution grids, the filaments
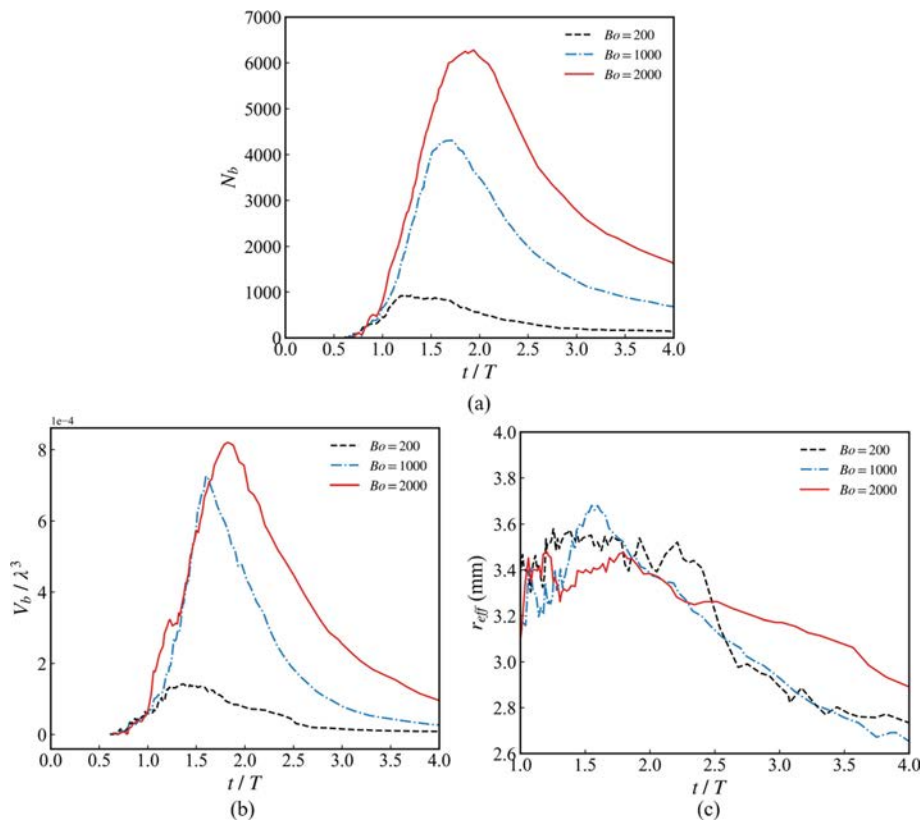
FIG. 35. Temporal evolution of bubble characteristics: (a) number of bubbles, (b) total bubble volume of bubbles, and (c) mean equivalent radius of bubbles.

remain attached to the main body of the bubble, preserving a slender trailing form. In contrast, coarse grids fail to resolve such fine-scale features, resulting in the detachment of these structures and the formation of isolated small bubbles. The rising velocity and centroid position of the bubble at various grid resolutions are shown in Fig. 32. It is evident that the results from finer grids, particularly $\Delta \geq D/64$, exhibit better agreement with the reference solution by Hysing *et al.,*[78] whereas coarser grids produce larger oscillation amplitudes and greater deviations.

3. Stokes wave breaking

A large amount of water–air–bubble mixed flow is generated during wave breaking. To investigate the influence of surface tension on bubble characteristics, a three-dimensional Stokes wave-breaking case with a wavelength of $\lambda = 1\,\text{m}$ is simulated.[26,46–48] As shown in Fig. 33, a third-order Stokes wave is initialized in a cubic computational domain with a side length of $1\,\text{m}$, with the wave profile remaining uniform along the spanwise direction The density and dynamic viscosity ratios between air and water are set to realistic values, $\rho_a/\rho_w = 1/998$, and $\mu_a/\mu_w = 1.784 \times 10^{-5}/1.138 \times 10^{-3}$, respectively. The effect of surface tension is quantified by varying the Bond number, $Bo = \Delta\rho g/(\sigma k^2)$, where $k = 2\pi/\lambda$ is the wavenumber. Adaptive mesh refinement is employed, with a minimum grid size of 2 mm used to simulate three cases: $Bo = 200$, 1000, and 2000.

Figure 34 shows the evolution of the free surface under different Bond numbers. It is evident that variations in surface tension lead to significantly different degrees of wave breaking. Larger Bond

numbers result in more violent surface fragmentation, with higher droplet splashes and increased air entrainment. Bubble characteristics are presented in Fig. 35. Figures 35(a) and 35(b) show the time histories of bubble number and bubble volume, respectively. It is observed that both the number and volume of bubbles increase with Bond numbers, and the peak values occur earlier at higher Bond numbers. Figure 35(c) shows the mean bubble radius. During the active breaking stage $t/T < 2$, the average bubble size for $Bo = 2000$ is smaller than that for $Bo = 200$ and 1000, reflecting the formation of more small-scale bubbles due to more intense fragmentation. In the later stage $t/T \geq 2$, the $Bo = 2000$ case exhibits more remaining large bubbles, leading to a larger average bubble size than other cases, as shown in Fig. 34(c). Although further analysis is required, these results indicate that surface tension plays a critical role in determining bubble characteristics. Therefore, accurate modeling of surface tension is essential when studying small-scale structures in wave-breaking flows.

REFERENCES

[1] J. Wang, Y. Shao, X. Li *et al.*, "Wave-breaking phenomena around a wedge-shaped bow," Phys. Fluids **37**(1), 012124 (2025).

[2] R. R. Dong, J. Katz, and T. T. Huang, "On the structure of bow waves on a ship model," J. Fluid Mech. **346**, 77–115 (1997).

[3] G. I. Roth, D. T. Mascenik, and J. Katz, "Measurements of the flow structure and turbulence within a ship bow wave," Phys. Fluids **11**(11), 3512–3523 (1999).

[4] J. Longo and F. Stern, "Effects of drift angle on model ship flow," Exp. Fluids **32**(5), 558–569 (2002).

[5] V. Hengelmolen and P. R. Wellens, "An experimental study on added resistance focused on the effects of bow wave breaking and relative wave measurements," Int. Shipbuild. Prog. **69**(1), 61–89 (2022).

[6] E. Baba, "A new component of viscous resistance of ships," J. Soc. Naval Archit. Jpn. **1969**, 23–34.

[7] A. Olivieri, F. Pistani, R. Wilson et al., "Scars and vortices induced by ship bow and shoulder wave breaking," J. Fluids Eng. **129**(11), 1445–1459 (2007).

[8] A. Olivieri, F. Pistani, and A. D. Mascio, "Breaking wave at the bow of a fast displacement ship model," J. Mar. Sci. Technol. **8**, 68–75 (2003).

[9] B. Choi, P. R. Wellens, and R. H. M. Huijsmans, "Experimental assessment of effects of bow-wave breaking on added resistance for the fast ship," Int. Shipbuild. Prog. **66**(2), 111–143 (2019).

[10] W. Liu, W. Wang, G. Qiu et al., "KCS unsteady bow wave breaking experiments for physics and CFD validation," in 34th Symposium on Naval Hydrodynamics (SNH), 2022.

[11] B. Mallat, G. Germain, J. Y. Billard et al., "A 3D study of the bubble sweep-down phenomenon around a 1/30 scale ship model," Eur. J. Mech., B: Fluids **72**, 471–484 (2018).

[12] B. Mallat, G. Germain, J.-Y. Billard et al., "Breaking wave bubble measurements around ship model by optical probe," Ocean Eng. **246**, 110438 (2022).

[13] M. Landrini, A. Colagrossi, M. Greco et al., "The fluid mechanics of splashing bow waves on ships: A hybrid BEM–SPH analysis," Ocean Eng. **53**, 111–127 (2012).

[14] S. Marrone, B. Bouscasse, A. Colagrossi et al., "Study of ship wave breaking patterns using 3D parallel SPH simulations," Comput. Fluids **69**, 54–66 (2012).

[15] J. Chen and X. Bai, "Analysis of sea spray generation and distribution characteristics in vessels with different bow shapes," Phys. Fluids **36**(1), 017142 (2024).

[16] C. W. Hirt and B. D. Nichols, "Volume of fluid (VOF) method for the dynamics of free boundaries," J. Comput. Phys. **39**(1), 201–225 (1981).

[17] J. Wang, Z. Ren, and D. Wan, "Study of a container ship with breaking waves at high Froude number using URANS and DDES methods," J. Ship Res. **64**(4), 346–356 (2020).

[18] J. H. Wang, W. T. Wang, and D. C. Wan, "Scale effects on bow wave breaking of KCS ship model: Insights from DDES investigations," J. Hydrodyn. **35**(4), 668–678 (2023).

[19] D. Wu, J. Wang, and D. Wan, "Delayed detached eddy simulation method for breaking bow waves of a surface combatant model with different trim angle," Ocean Eng. **242**, 110177 (2021).

[20] S. Osher and R. P. Fedkiw, "Level set methods: An overview and some recent results," J. Comput. Phys. **169**(2), 463–502 (2001).

[21] R. V. Wilson, P. M. Carrica, and F. Stern, "URANS simulations for a high-speed transom stern ship with breaking waves," Int. J. Comput. Fluid Dyn. **20**(2), 105–125 (2006).

[22] P. M. Carrica, R. V. Wilson, R. W. Noack et al., "Ship motions using single-phase level set with dynamic overset grids," Comput. Fluids **36**(9), 1415–1433 (2007).

[23] A. Mascio, R. Broglia, and R. Muscari, "On the application of the single-phase level set method to naval hydrodynamic flows," Comput. Fluids **36**(5), 868–886 (2007).

[24] M. Sussman and E. G. Puckett, "A coupled level set and volume-of-fluid method for computing 3D and axisymmetric incompressible two-phase flows," J. Comput. Phys. **162**(2), 301–337 (2000).

[25] S. Mirjalili, S. S. Jain, and M. Dodd, "Interface-capturing methods for two-phase flows: An overview and recent developments," Center for Turbulence Research: Annual Research Briefs (Stanford Engineering, Stanford, CA, 2017), Vol. 13, pp. 117–135.

[26] Z. Wang, J. Yang, and F. Stern, "High-fidelity simulations of bubble, droplet and spray formation in breaking waves," J. Fluid Mech. **792**, 307–327 (2016).

[27] Z. Li, C. Liu, D. Wan, and C. Hu, "High-fidelity simulation of a hydraulic jump around a surface-piercing hydrofoil," Phys. Fluids **33**(12), 123304 (2021).

[28] F. Noblesse, G. Delhommeau, P. Queutey et al., "An elementary analytical theory of overturning ship bow waves," Eur. J. Mech., B: Fluids **48**, 193–209 (2014).

[29] F. Noblesse, D. Hendrix, L. Faul et al., "Simple analytical expressions for the height, location, and steepness of a ship bow wave," J. Ship Res. **50**(4), 360–370 (2006).

[30] F. Noblesse, G. E. R. Delhommeau, M. Guilbaud et al., "Simple analytical relations for ship bow waves," J. Fluid Mech. **600**, 105–132 (2008).

[31] F. Noblesse, G. Delhommeau, H. Liu et al., "Ship bow waves," J. Hydrodyn. **25**(4), 491–501 (2013).

[32] Y. Hu, C. Liu, C. Hu et al., "Numerical investigation of flow structure and air entrainment of breaking bow wave generated by a rectangular plate," Phys. Fluids **33**(12), 122113 (2021).

[33] Y. Hu, C. Liu, M. Zhao et al., "High-fidelity simulation of an aerated cavity around a surface-piercing rectangular plate," Phys. Rev. Fluids **8**(4), 044003 (2023).

[34] C. M. Harwood, Y. L. Young, and S. L. Ceccio, "Ventilated cavities on a surface-piercing hydrofoil at moderate Froude numbers: Cavity formation, elimination and stability," J. Fluid Mech. **800**, 5–56 (2016).

[35] R. Huang, R. Qiu, Y. Zhi et al., "Investigations into the ventilated cavities around a surface-piercing hydrofoil at high Froude numbers," Phys. Fluids **34**(4), 043304 (2022).

[36] J. Huang, J. Wang, X. Lu et al., "Hydrodynamic performance of a surface-piercing hydrofoil with differing oblique angle: A numerical study," Phys. Fluids **36**(12), 123354 (2024).

[37] Y. Zhi, R. Huang, R. Qiu et al., "Numerical investigation of the tip-vortex-induced ventilation formation mechanism for a surface-piercing hydrofoil," Phys. Fluids **35**(12), 123328 (2023).

[38] Y. Zhi, R. Huang, R. Qiu et al., "LES investigation into the cavity shedding dynamics and cavitation–vortex interaction around a surface-piercing hydrofoil," Phys. Fluids **34**(12), 123314 (2022).

[39] A. Waniewski, C. E. Brennen, and F. Raichlen, "Bow wave dynamics," J. Ship Res. **46**(1), 1–15 (2002).

[40] A. Waniewski, "Air entrainment by bow waves," Doctoral dissertation (California Institute of Technology, Pasadena, California, 1999).

[41] T. A. Waniewski, C. E. Brennen, and F. Raichlen, "Measurements of air entrainment by bow waves," J. Fluids Eng. **123**(1), 57–63 (2001).

[42] A. Karion, T. C. Fu, T. Waniewski-Sur, J. R. Rice, D. C. Walker, and D. A. Furey, "Experiment to examine the effect of scale on a breaking bow wave" (Hydromechanics Department, Naval Surface Warfare Center, Carderock Division, 2004).

[43] Z. Wang, J. Yang, and F. Stern, "Numerical simulations of wave breakings around a wedge-shaped bow," in 28th Symposium on Naval Hydrodynamics, Pasadena, California, 2010.

[44] G. B. Deane and M. D. Stokes, "Scale dependence of bubble creation mechanisms in breaking waves," Nature **418**(6900), 839–844 (2002).

[45] L. Deike, "Mass transfer at the ocean–atmosphere interface: The role of wave breaking, droplets, and bubbles," Annu. Rev. Fluid Mech. **54**(1), 191–224 (2022).

[46] L. Deike, S. Popinet, and W. K. Melville, "Capillary effects on wave breaking," J. Fluid Mech. **769**, 541–569 (2015).

[47] C. Liu, Y. Hu, X. Yang et al., "Numerical study of bubble rise in plunging breaking waves," Phys. Fluids **36**(5), 052111 (2024).

[48] W. Mostert, S. Popinet, and L. Deike, "High-resolution direct simulation of deep water breaking waves: Transition to turbulence, bubbles and droplets production," J. Fluid Mech. **942**, A27 (2022).

[49] B. Wang, X. Guo, H. Liu, and C. He, "Numerical simulations of wake signatures around high-speed ships," J. Hydrodyn. **26**(6), 986–989 (2014).

[50] Y. Yang, Y. Hu, C. Liu, R. Gao, and C. Hu, "Wake and air entrainment properties of transom stern over a wide range of Froude numbers," Phys. Fluids **35**(6), 062110 (2023).

[51] S. Popinet, "An accurate adaptive solver for surface-tension-driven interfacial flows," J. Comput. Phys. **228**(16), 5838–5866 (2009).

[52] S. Popinet, "A quadtree-adaptive multigrid solver for the Serre–Green–Naghdi equations," J. Comput. Phys. **302**, 336–358 (2015).

[53] K. Zinelis, T. Abadie, G. H. McKinley, and O. K. Matar, "Transition to elasto-capillary thinning dynamics in viscoelastic jets," J. Fluid Mech. **998**, A4 (2024).

[54] S. Zhao, J. Zhang, C. Sun, and M.-J. Ni, "Direct numerical simulations of Leidenfrost drop impacting onto superheated liquid pool: An early stage study," J. Fluid Mech. **1007**, A13 (2025).

[55] Y. Shao, W. Wang, D. Wan, and J. Wang, "Numerical investigations of breaking waves and air entrainment induced by a shallowly submerged hydrofoil," Ocean Eng. **312**, 119026 (2024).

[56] Y. M. Shao, W. T. Wang, G. L. Zhang, J. H. Wang, and D. C. Wan, "Numerical simulations of breaking waves generated by a 3-D submerged hydrofoil," J. Hydrodyn. **37**(1), 35–49 (2025).

23 July 2025 00:17:37

[57] K. Patel, J. Sun, Z. Yang, and X. Zhu, "Coupled liquid–gas flow over a submerged cylinder: Interface topology, wake structure and hydrodynamic lift," J. Fluid Mech. **1008**, A10 (2025).

[58] W. Zhang, M. Wang, W. Zhao, and D. Wan, "Numerical analysis of air entrainment and flows around a surface-piercing finite circular cylinder," Phys. Fluids **37**(3), 032127 (2025).

[59] M. Ji, Y. Han, L. Jin, Y. Wu, Y. Wang, and Y. Kuai, "Numerical simulation on the characteristics of interface breakup and entrained bubble distribution around ship under quasi-stationary state," Phys. Fluids **37**(4), 043354 (2025).

[60] A. W. Vreman, "An eddy-viscosity subgrid-scale model for turbulent shear flow: Algebraic theory and applications," Phys. Fluids **16**(10), 3670–3681 (2004).

[61] S. Popinet, "Numerical models of surface tension," Annu. Rev. Fluid Mech. **50**, 49–75 (2018).

[62] J. Yang and F. Stern, "Sharp interface immersed-boundary/level-set method for wave–body interactions," J. Comput. Phys. **228**(17), 6590–6616 (2009).

[63] J. Yang and F. Stern, "A simple and efficient direct forcing immersed boundary framework for fluid–structure interactions," J. Comput. Phys. **231**(15), 5029–5061 (2012).

[64] A. Limare, S. Popinet, C. Josserand, Z. Xue, and A. Ghigo, "A hybrid level-set/embedded boundary method applied to solidification-melt problems," J. Comput. Phys. **474**, 111829 (2023).

[65] Z. Lin-Lin, G. Hui, and W. Chui-Jie, "Three-dimensional numerical simulation of a bird model in unsteady flight," Comput. Mech. **58**, 1–11 (2016).

[66] M. Tavares, C. Josserand, A. Limare, J. M. Lopez-Herrera, and S. Popinet, "A coupled VOF/embedded boundary method to model two-phase flows on arbitrary solid surfaces," Comput. Fluids **278**, 106317 (2024).

[67] A. R. Ghigo, S. Popinet, and A. Wachs, see https://hal.science/hal-03948786 for "A Conservative Finite Volume Cut-Cell Method on an Adaptive Cartesian Tree Grid for Moving Rigid Bodies in Incompressible Flows" (2021).

[68] X. Chen, T. Han, J. Pan, D. Fuster, and S. Zaleski, "Volume-conserving method for dynamic contact line on complex surfaces," Phys. Fluids **37**(2), 023392 (2025).

[69] K. Hendrickson, G. D. Weymouth, X. Yu, and D. K. P. Yue, "Wake behind a three-dimensional dry transom stern. Part 1. Flow structure and large-scale air entrainment," J. Fluid Mech. **875**, 854–883 (2019).

[70] Z. Wang and F. Stern, "Moving air-water interface on no-slip solid walls for high-speed planing hulls," Ships Offshore Struct. **20**, 732–738 (2025).

[71] R. Li, Z. Yang, and W. Zhang, "Numerical investigation of mixed-phase turbulence induced by a plunging jet," J. Fluid Mech. **979**, A27 (2024).

[72] Z. Li, X. S. Zhang, and D. C. Wan, "Research progress on the hydrodynamic performance of water-air-bubble mixed flows around a ship," J. Hydrodyn. **34**(2), 171–188 (2022).

[73] M. A. Erinin, C. Liu, S. D. Wang, X. Liu, and J. H. Duncan, "Plunging breakers. Part 2. Droplet generation," J. Fluid Mech. **967**, A36 (2023).

[74] M. R. Loewen, M. A. O'Dor, and M. G. Skafel, "Bubbles entrained by mechanically generated breaking waves," J. Geophys. Res. **101**(C9), 20759–20769, https://doi.org/10.1029/96JC01919 (1996).

[75] J. W. Cartmill and M. Y. Su, "Bubble size distribution under saltwater and freshwater breaking waves," Dyn. Atmos. Oceans **20**(1–2), 25–31 (1993).

[76] B. Metcalf, J. Longo, S. Ghosh, and F. Stern, "Unsteady free-surface wave-induced boundary-layer separation for a surface-piercing NACA 0024 foil: Towing tank experiments," J. Fluids Struct. **22**(1), 77–98 (2006).

[77] M. Zhang, H. Hu, B. Guo, Q. Liang, F. Zhang, X. Chen, Z. Xie, and P. Du, "Predicting shear stress distribution on structural surfaces under internal solitary wave loading: A deep learning perspective," Phys. Fluids **36**(3), 035153 (2024).

[78] S. Hysing, S. Turek, D. Kuzmin, N. Parolini, E. Burman, S. Ganesan, and L. Tobiska, "Quantitative benchmark computations of two-dimensional bubble dynamics," Int. J. Numer. Methods Fluids **60**(11), 1259–1288 (2009).

23 July 2025 00:17:37